

Novel Adaptive Schemes for Hyperbolic Conservation Laws

Shaoshuai Chu*, Pingyao Feng†, Vadim A. Kolotilov‡,

Alexander Kurganov§ and Vladimir V. Ostapenko ¶

Abstract

We introduce new adaptive schemes for the one- and two-dimensional hyperbolic systems of conservation laws. Our schemes are based on an adaption strategy recently introduced in [S. CHU, A. KURGANOV, AND I. MENSHOV, Appl. Numer. Math., 209 (2025)]. As there, we use a smoothness indicator (SI) to automatically detect “rough” parts of the solution and employ in those areas the second-order finite-volume low-dissipation central-upwind scheme with an overcompressive limiter, which helps to sharply resolve nonlinear shock waves and linearly degenerate contact discontinuities. In smooth parts, we replace the limited second-order scheme with a quasi-linear fifth-order (in space and third-order in time) finite-difference scheme, recently proposed in [V. A. KOLOTOLOV, V. V. OSTAPENKO, AND N. A. KHANDEEVA, Comput. Math. Math. Phys., 65 (2025)]. However, direct application of this scheme may generate spurious oscillations near “rough” parts, while excessive use of the overcompressive limiter may cause staircase-like nonphysical structures in smooth areas. To address these issues, we employ the same SI to distinguish contact discontinuities, treated with the overcompressive limiter, from other “rough” regions, where we switch to the dissipative Minmod2 limiter. Advantage of the resulting adaptive schemes are clearly demonstrated on a number of challenging numerical examples.

Key words: Adaptive schemes; low-dissipation central-upwind numerical fluxes; smoothness indicator; overcompressive and dissipative limiters; quasi-linear fifth-order finite-difference scheme; Euler equations of gas dynamics.

AMS subject classification: 65M08, 65M06, 76M12, 76M20, 76L05, 35L65.

1 Introduction

We consider hyperbolic systems of conservation laws, which in the one-dimensional (1-D) and two-dimensional (2-D) cases, read as

$$\mathbf{U}_t + \mathbf{F}(\mathbf{U})_x = \mathbf{0}, \quad (1.1)$$

and

$$\mathbf{U}_t + \mathbf{F}(\mathbf{U})_x + \mathbf{G}(\mathbf{U})_y = \mathbf{0}, \quad (1.2)$$

*Department of Mathematics, RWTH Aachen University, 52056 Aachen, Germany; chu@igpm.rwth-aachen.de

†Department of Mathematics, North Carolina State University, 27695 Raleigh, USA; pfeng3@ncsu.edu

‡Lavrentyev Institute of Hydrodynamics, Siberian Branch, Russian Academy of Sciences, Novosibirsk, 630090 Russia; kolotilov1992@gmail.com

§Department of Mathematics and Shenzhen International Center for Mathematics, Southern University of Science and Technology, Shenzhen, 518055, China; alexander@sustech.edu.cn

¶Lavrentyev Institute of Hydrodynamics, Siberian Branch, Russian Academy of Sciences, Novosibirsk, 630090 Russia; ostapenko_vv@ngs.ru

respectively. Here, x and y are spatial variables, t is the time, $\mathbf{U} \in \mathbb{R}^d$ is a vector of unknown functions, and $\mathbf{F} : \mathbb{R}^d \rightarrow \mathbb{R}^d$ and $\mathbf{G} : \mathbb{R}^d \rightarrow \mathbb{R}^d$ are fluxes.

It is well-known that solutions of (1.1) and (1.2) can produce extremely complex wave structures including shocks, rarefactions, and contact discontinuities even when the initial data are smooth. This makes it quite challenging to develop accurate and reliable numerical methods for (1.1) and (1.2). Such methods are typically based on equivalent integral forms of (1.1) and (1.2) for the time evolution of the computed solution and on nonlinear limiters, designed to prevent spurious oscillations. For a variety of existing numerical methods for hyperbolic systems of conservation laws, we refer the reader to the monographs and review papers [2, 17, 21, 27, 39, 42] and references therein.

In this paper, we focus on scheme adaption methods, which are based on automatic detection of smooth and nonsmooth (“rough”) parts of the computed solutions and on applying different numerical methods in the corresponding parts of the computational domain. The main advantage of such an approach is related to the fact that special nonlinear limiting techniques can be used to accurately capture shock waves and contact discontinuities only, while smooth parts of the solution may be accurately and efficiently computed by much simpler, possibly higher-order, (quasi-linear) unlimited methods.

A success of adaptive schemes hinges on an accuracy and robustness of the smoothness indicator (SI) used to detect “rough” parts of the computed solution. A wide variety of different SIs has been developed; see, e.g., [1, 6, 11–16, 20, 22, 30, 31, 33, 43–45]. Another critical component of a successful adaptive scheme is a very sharp method used to capture shock and contact discontinuities inside the identified “rough” parts of the solution. In this paper, we follow [8] and implement the SI proposed in [30] along with the second-order semi-discrete finite-volume low-dissipation central-upwind (LDCU) schemes from [10] combined with the overcompressive and dissipative limiters introduced in [28].

The novelty of the proposed adaptive schemes is twofold. First, we treat the smooth parts of the computed solutions in a different way. Instead of using the second-order LDCU scheme with the dissipative Minmod2 limiter (see [28] for the classification of different limiters) as it was done in [8], we increase the resolution by switching to the recently proposed quasi-linear fifth-order (in space and third-order in time) finite-difference scheme recently introduced in [24]. Following [26], we call a numerical scheme *quasi-linear* if it becomes linear when applied to linear hyperbolic systems. As it was shown in [24], the fifth-order quasi-linear scheme is very accurate and like the third-order Rusanov-Burstein-Mirin scheme [4, 34], it achieves increased accuracy in shock influence regions. This scheme, however, does not contain any nonlinear stabilization mechanism and thus cannot be used in the “rough” areas. Moreover, as we show in §2.3, it can produce spurious oscillations near the interfaces between the “rough” and “smooth” regions. To suppress these oscillations, one can “enlarge” the identified “rough” areas, but in this case, the overcompressive limiter would affect the smooth parts of the solution causing development of artificial kinks and staircase-like structures or even nonphysical jump discontinuities there.

In order to address these issues, we introduce an alternative approach, which is the second novel component of the proposed adaptive schemes. To this end, we use the same SI, but applied to different fields to automatically distinguish between the contact waves and other “rough” parts of the solution. For example, in the case of Euler equations of gas dynamics, we take advantage of the fact that while the density jumps at the contact surfaces, the pressure remains continuous there. After identifying the locations of contact surfaces, we apply the second-order LDCU scheme with an overcompressive limiter in their vicinities only, while utilizing the dissipative Minmod2 limiter in the rest of the “rough” areas. In addition, the overcompressive and Minmod2 limiters are applied to the local characteristic variables using the local characteristic decomposition (LCD), which is often used in the context of high-order schemes [32] to suppress spurious oscillations, but can also be implemented to enhance the resolution of second-order schemes; see, e.g., [7, 9]. This way, we construct efficient and robust adaptive schemes, which achieve a very high resolution of both jump discontinuities and smooth parts of the computed solutions.

The paper is organized as follows. In §2, we review the 1-D LDCU scheme from [10], the fifth-order finite-difference scheme from [24], and then introduce a 1-D adaptive scheme based on the scheme

adaption strategy from [8]. We also demonstrate that the obtained adaptive scheme is not robust and thus it has to be modified. In §3, we present a new 1-D adaptive scheme, which is based on the dynamical splitting of the computational domains into three parts: vicinities of the contact discontinuities, other “rough” parts of the computed solutions, and smooth parts of the computed solutions. In §4, we extend the new adaptive scheme to the 2-D case. In §5, we test the developed schemes on a number of 1-D and 2-D numerical examples for the Euler equations of gas dynamics. The obtained numerical results demonstrate that the adaptive schemes contain a substantially smaller amount of numerical dissipation and achieve higher resolution compared with the adaptive schemes from [8]. Finally, in §6, we provide concluding remarks.

2 1-D Scheme Adaption Algorithm

In this section, we consider the 1-D hyperbolic system (1.1) and describe a scheme adaption algorithm similar to the one recently introduced in [8]. The novel feature here is in the treatment of smooth parts of the computed areas detected by the SI; see §2.2 and §2.3.

2.1 1-D Low-Dissipation Central-Upwind (LDCU) Schemes

In this section, we briefly review the second-order semi-discrete LDCU schemes recently introduced in [10].

Assuming that the computational domain is covered with the uniform cells $I_j := [x_{j-\frac{1}{2}}, x_{j+\frac{1}{2}}]$ with $x_{j+\frac{1}{2}} - x_{j-\frac{1}{2}} \equiv \Delta x$ centered at $x_j = (x_{j-\frac{1}{2}} + x_{j+\frac{1}{2}})/2$, we suppose that the computed cell averages,

$$\bar{\mathbf{U}}_j(t) := \frac{1}{\Delta x} \int_{I_j} \mathbf{U}(x, t) dx,$$

are available at a certain time level $t \geq 0$. Note that $\bar{\mathbf{U}}_j(t)$ like many other indexed quantities, which will be introduced below, are time-dependent, but from here on, we suppress their time-dependence for the sake of brevity.

The computed cell averages are evolved in time by numerically solving the following system of ODEs:

$$\frac{d\bar{\mathbf{U}}_j}{dt} = -\frac{\mathcal{F}_{j+\frac{1}{2}}[\mathbf{U}] - \mathcal{F}_{j-\frac{1}{2}}[\mathbf{U}]}{\Delta x}, \quad (2.1)$$

where $\mathcal{F}_{j+\frac{1}{2}}[\mathbf{U}]$ are the LDCU numerical fluxes given by (see [10])

$$\mathcal{F}_{j+\frac{1}{2}}[\mathbf{U}] = \frac{a_{j+\frac{1}{2}}^+ \mathbf{F}(\mathbf{U}_{j+\frac{1}{2}}^-) - a_{j+\frac{1}{2}}^- \mathbf{F}(\mathbf{U}_{j+\frac{1}{2}}^+)}{a_{j+\frac{1}{2}}^+ - a_{j+\frac{1}{2}}^-} + \frac{a_{j+\frac{1}{2}}^+ a_{j+\frac{1}{2}}^-}{a_{j+\frac{1}{2}}^+ - a_{j+\frac{1}{2}}^-} (\mathbf{U}_{j+\frac{1}{2}}^+ - \mathbf{U}_{j+\frac{1}{2}}^-) + \mathbf{q}_{j+\frac{1}{2}}.$$

Here:

- $\mathbf{U}_{j+\frac{1}{2}}^\pm$ are the left- and right-sided point values of \mathbf{U} at the cell interface $x = x_{j+\frac{1}{2}}$ reconstructed out of the given set of cell averages $\{\bar{\mathbf{U}}_j\}$ using a proper nonlinear limiter; see Appendix A;
- $a_{j+\frac{1}{2}}^\pm$ are the one-sided local speeds of propagation, which can be estimated using the largest and smallest eigenvalues of the Jacobian $A(\mathbf{U}) := \frac{\partial \mathbf{F}}{\partial \mathbf{U}}(\mathbf{U})$;
- $\mathbf{q}_{j+\frac{1}{2}}$ is a “built-in” anti-diffusion term, which needs to be derived for a particular system at hand.

In this paper, we consider the Euler equations of gas dynamics, which, in the 1-D case, read as (1.1) with

$$\mathbf{U} = (\rho, \rho u, E)^\top \quad \text{and} \quad \mathbf{F} = (\rho u, \rho u^2 + p, u(E + p))^\top. \quad (2.2)$$

Here, ρ , u , p , and E are the density, velocity, pressure, and total energy, respectively, and the system is closed through the following equations of state (EOS) for ideal gases:

$$p = (\gamma - 1) \left[E - \frac{1}{2} \rho u^2 \right], \quad (2.3)$$

where the parameter γ represents the specific heat ratio. For the Euler system (1.1), (2.2)–(2.3), the one-sided local speeds of propagation can be estimated by

$$a_{j+\frac{1}{2}}^+ = \max \left\{ u_{j+\frac{1}{2}}^+ + c_{j+\frac{1}{2}}^+, u_{j+\frac{1}{2}}^- + c_{j+\frac{1}{2}}^-, 0 \right\}, \quad a_{j+\frac{1}{2}}^- = \min \left\{ u_{j+\frac{1}{2}}^+ - c_{j+\frac{1}{2}}^+, u_{j+\frac{1}{2}}^- - c_{j+\frac{1}{2}}^-, 0 \right\},$$

where

$$u_{j+\frac{1}{2}}^\pm = \frac{(\rho u)_{j+\frac{1}{2}}^\pm}{\rho_{j+\frac{1}{2}}^\pm}, \quad p_{j+\frac{1}{2}}^\pm = (\gamma - 1) \left[E_{j+\frac{1}{2}}^\pm - \frac{1}{2} \rho_{j+\frac{1}{2}}^\pm (u_{j+\frac{1}{2}}^\pm)^2 \right], \quad c_{j+\frac{1}{2}}^\pm = \sqrt{\frac{\gamma p_{j+\frac{1}{2}}^\pm}{\rho_{j+\frac{1}{2}}^\pm}},$$

and the anti-diffusion term $\mathbf{q}_{j+\frac{1}{2}}$ is given by (see [10])

$$\mathbf{q}_{j+\frac{1}{2}} = \alpha_{j+\frac{1}{2}}^* q_{j+\frac{1}{2}}^\rho \left(1, u_{j+\frac{1}{2}}^*, \frac{1}{2} (u_{j+\frac{1}{2}}^*)^2 \right)^\top.$$

Here,

$$q_{j+\frac{1}{2}}^\rho = \text{minmod} \left((u_{j+\frac{1}{2}}^* - a_{j+\frac{1}{2}}^-)(\rho_{j+\frac{1}{2}}^* - \rho_{j+\frac{1}{2}}^-), (a_{j+\frac{1}{2}}^+ - u_{j+\frac{1}{2}}^*)(\rho_{j+\frac{1}{2}}^+ - \rho_{j+\frac{1}{2}}^*) \right),$$

$u_{j+\frac{1}{2}}^* = (\rho u)_{j+\frac{1}{2}}^*/\rho_{j+\frac{1}{2}}^*$ with $\rho_{j+\frac{1}{2}}^*$ and $(\rho u)_{j+\frac{1}{2}}^*$ being the first and second components of

$$\mathbf{U}_{j+\frac{1}{2}}^* = \frac{a_{j+\frac{1}{2}}^+ \mathbf{U}_{j+\frac{1}{2}}^+ - a_{j+\frac{1}{2}}^- \mathbf{U}_{j+\frac{1}{2}}^- - [\mathbf{F}(\mathbf{U}_{j+\frac{1}{2}}^+) - \mathbf{F}(\mathbf{U}_{j+\frac{1}{2}}^-)]}{a_{j+\frac{1}{2}}^+ - a_{j+\frac{1}{2}}^-},$$

$$\alpha_{j+\frac{1}{2}}^* = \begin{cases} \frac{a_{j+\frac{1}{2}}^+}{a_{j+\frac{1}{2}}^+ - u_{j+\frac{1}{2}}^*} & \text{if } u_{j+\frac{1}{2}}^* < 0, \\ \frac{a_{j+\frac{1}{2}}^-}{a_{j+\frac{1}{2}}^- - u_{j+\frac{1}{2}}^*} & \text{otherwise,} \end{cases}$$

and the minmod function is defined by $\text{minmod}(a, b) := \frac{\text{sgn}(a) + \text{sgn}(b)}{2} \min(|a|, |b|)$.

Remark 2.1 The ODE system (2.1) has to be numerically integrated using a sufficiently accurate and stable ODE solver. In the numerical examples reported in this paper, we have used the three-stage third-order strong stability preserving (SSP) Runge-Kutta method, which reads as (see [18, 19])

$$\begin{aligned} \mathbf{U}_j^I &= \mathbf{U}_j(t) - \frac{\Delta t}{\Delta x} \left(\mathcal{F}_{j+\frac{1}{2}}[\mathbf{U}(t)] - \mathcal{F}_{j-\frac{1}{2}}[\mathbf{U}(t)] \right), \\ \mathbf{U}_j^{II} &= \frac{3}{4} \mathbf{U}_j(t) + \frac{1}{4} \left[\mathbf{U}_j^I - \frac{\Delta t}{\Delta x} \left(\mathcal{F}_{j+\frac{1}{2}}[\mathbf{U}^I] - \mathcal{F}_{j-\frac{1}{2}}[\mathbf{U}^I] \right) \right], \\ \mathbf{U}_j(t + \Delta t) &= \frac{1}{3} \mathbf{U}_j(t) + \frac{2}{3} \left[\mathbf{U}_j^{II} - \frac{\Delta t}{\Delta x} \left(\mathcal{F}_{j+\frac{1}{2}}[\mathbf{U}^{II}] - \mathcal{F}_{j-\frac{1}{2}}[\mathbf{U}^{II}] \right) \right]. \end{aligned} \quad (2.4)$$

In (2.4), the time step Δt is selected adaptively based on the following CFL-based stability restriction:

$$\Delta t \leq \frac{\Delta x}{2a}, \quad a := \max_j \left\{ \max(a_{j+\frac{1}{2}}^+, -a_{j+\frac{1}{2}}^-) \right\}.$$

Notice that in (2.4) we have replaced the cell averages of \mathbf{U} with its point values ($\mathbf{U}_j(t) \approx \mathbf{U}(x_j, t^n)$). This does not affect the accuracy of the second-order scheme as the difference between the cell averages and point values is proportional to $\mathcal{O}((\Delta x)^2)$ for smooth solutions. On the other hand, switching to the finite-difference evolution is advantageous as the LDCU scheme is going to be combined with the quasi-linear fifth-order finite-difference scheme from [24], for which the point values of the solution are to be evolved in time.

2.2 1-D Quasi-Linear Fifth-Order Scheme

In this section, we describe the quasi-linear fifth-order finite-difference scheme recently introduced in [24]. As this scheme is going to be implemented in our adaption algorithm, we write it in the fully discrete flux form (2.4).

Assuming the point values \mathbf{U}_j are available at a certain time level t , the solution is evolved to the next time level $t + \Delta t$ according to (2.4) with the following numerical fluxes:

$$\mathcal{F}_{j+\frac{1}{2}}[\mathbf{U}(t)] = \mathcal{L}_{j+\frac{1}{2}}[\mathbf{U}(t)], \quad \mathcal{F}_{j+\frac{1}{2}}[\mathbf{U}^I] = \mathcal{L}_{j+\frac{1}{2}}[\mathbf{U}^I], \quad \mathcal{F}_{j+\frac{1}{2}}[\mathbf{U}^{II}] = \mathcal{L}_{j+\frac{1}{2}}[\mathbf{U}^{II}] - \boldsymbol{\omega}_{j+\frac{1}{2}}(t),$$

where

$$\begin{aligned} \mathcal{L}_{j+\frac{1}{2}}[\mathbf{U}] &:= \frac{1}{60} [\mathbf{F}(\mathbf{U}_{j+3}) - 8\mathbf{F}(\mathbf{U}_{j+2}) + 37\mathbf{F}(\mathbf{U}_{j+1}) + 37\mathbf{F}(\mathbf{U}_j) - 8\mathbf{F}(\mathbf{U}_{j-1}) + \mathbf{F}(\mathbf{U}_{j-2})], \\ \boldsymbol{\omega}_{j+\frac{1}{2}}(t) &:= \frac{3\Delta x}{128\Delta t} [\mathbf{U}_{j+3}(t) - 5\mathbf{U}_{j+2}(t) + 10\mathbf{U}_{j+1}(t) - 10\mathbf{U}_j(t) + 5\mathbf{U}_{j-1}(t) - \mathbf{U}_{j-2}(t)]. \end{aligned}$$

In the next numerical example, we demonstrate that the described 1-D quasi-linear scheme achieves the fifth order of accuracy in capturing a smooth solution provided $\Delta t \sim (\Delta x)^{\frac{5}{3}}$.

Example. We consider the following smooth initial data [23]:

$$u(x, 0) = \sin\left(\frac{\pi x}{5} + \frac{\pi}{4}\right), \quad \rho(x, 0) = \left[\frac{\gamma - 1}{2\sqrt{\gamma}} (u(x, 0) + 10)\right]^{\frac{2}{\gamma-1}}, \quad p(x, 0) = \rho^\gamma(x, 0),$$

subject to the periodic boundary conditions in the computational domain $[0, 10]$. We compute the numerical solution until the final time $t = 0.1$ on a sequence of uniform meshes with $\Delta x = 1/10, 1/20, 1/40, 1/80, 1/160$, and $1/320$.

We then compute the L^1 -errors and estimate the experimental convergence rates using the following Runge formulae, which are based on the solutions computed on the three consecutive uniform grids with the mesh sizes Δx , $2\Delta x$, and $4\Delta x$ and denoted by $(\cdot)^{\Delta x}$, $(\cdot)^{2\Delta x}$, and $(\cdot)^{4\Delta x}$, respectively:

$$\text{Error}(\Delta x) \approx \frac{\delta_{12}^2}{|\delta_{12} - \delta_{24}|}, \quad \text{Rate}(\Delta x) \approx \log_2 \left(\frac{\delta_{24}}{\delta_{12}} \right).$$

Here, $\delta_{12} := \|(\cdot)^{\Delta x} - (\cdot)^{2\Delta x}\|_{L^1}$ and $\delta_{24} := \|(\cdot)^{2\Delta x} - (\cdot)^{4\Delta x}\|_{L^1}$. The obtained results are reported in Table 2.1, where one can clearly see that the fifth order of accuracy is achieved.

2.3 1-D Adaptive Scheme

In this section, we turn to the description of the adaptive scheme from [8], in which we modify the treatment of the smooth part of the computed solution: we will evolve it using the quasi-linear fifth-order scheme from [24] instead of the LDCU scheme with the dissipative Minmod2 limiter. The “rough” parts of the computed solution will be still integrated using the LDCU scheme with the overcompressive ($\tau = -0.25$) limiter described in Appendix A.

Δx	ρ		ρu		E	
	Error	Rate	Error	Rate	Error	Rate
1/40	1.84e-07	4.76	6.03e-07	4.76	2.67e-06	4.76
1/80	4.89e-09	4.99	1.59e-08	5.00	7.06e-08	5.00
1/160	1.56e-10	4.98	5.11e-10	4.98	2.26e-09	4.98
1/320	5.05e-12	4.97	1.65e-11	4.97	7.30e-11	4.97

Table 2.1: The L^1 -errors and experimental convergence rates for ρ , ρu , and E computed by the quasi-linear fifth-order scheme.

In order to implement this scheme adaption strategy, we use the SI proposed in [30] (see also [8, §2.2]), which is based on the quantities

$$\mathcal{E}_j^\rho = \frac{|\rho_{j+1} - 2\rho_j + \rho_{j-1}|}{|\rho_{j+1} - \rho_j| + |\rho_j - \rho_{j-1}| + \varepsilon(\rho_{j+1} + 2\rho_j + \rho_{j-1})}, \quad (2.5)$$

which we smooth out in the following way:

$$\bar{\mathcal{E}}_j^\rho = \frac{1}{6}[\mathcal{E}_{j+1}^\rho + 4\mathcal{E}_j^\rho + \mathcal{E}_{j-1}^\rho]. \quad (2.6)$$

The term with ε in (2.5) plays the role of a “noise” filter, which is added in order not to refine “wiggles” or “ripples” that may appear due to loss of monotonicity; see [30]. The value of ε depends on the problem at hand and in all of the numerical examples presented in this paper, we use the same value $\varepsilon = 0.2$ as in [8, 30].

As in [8], we use the following simple way to detect “rough” parts of the computed solutions: If $\bar{\mathcal{E}}_j^\rho \geq C_1$, the cell I_j is marked as “rough”. Here, C_1 is a positive tunable constant to be selected for each problem at hand. The key component in making the adaptive scheme robust is the ability of finding a reliable range of constant C_1 values. As shown in [8], the value of C_1 can be tuned on a coarse mesh and then the same values can be used for finer mesh simulations.

We have tested the resulting adaptive scheme on a number of numerical examples and obtained fairly accurate and non-oscillatory results in some of them. However, there were some examples, in which this adaptive scheme was unable to produce satisfactory results. We now show one of such examples.

Example—Shock-Density Wave Interaction Problem. In this example taken from [41], we consider the shock-density wave interaction problem. The initial data,

$$(\rho, u, p)\Big|_{(x,0)} = \begin{cases} \left(\frac{27}{7}, \frac{4\sqrt{35}}{9}, \frac{31}{3}\right), & x < -4, \\ (1 + 0.2 \sin(5x), 0, 1), & x > -4, \end{cases}$$

are prescribed in the computational domain $[-5, 15]$ subject to the free boundary conditions.

We first compute the numerical solutions on a uniform mesh with $\Delta x = 1/40$ until the final time $t = 5$ by the adaptive scheme from [8], which will be referred to as the OLD scheme, and the adaptive scheme introduced in this section (this scheme will be referred to as the MODIFIED scheme). For both schemes, we use the adaption constant $C_1 = 0.004$. We present the obtained densities in Figure 2.1 together with the reference solution computed by the LDCU scheme (with $\tau = 0.5$ in (A.3)) on a much finer mesh with $\Delta x = 1/800$. One can see that compared with the OLD scheme, the MODIFIED one produces a more accurate result; see Figure 2.1 (right).

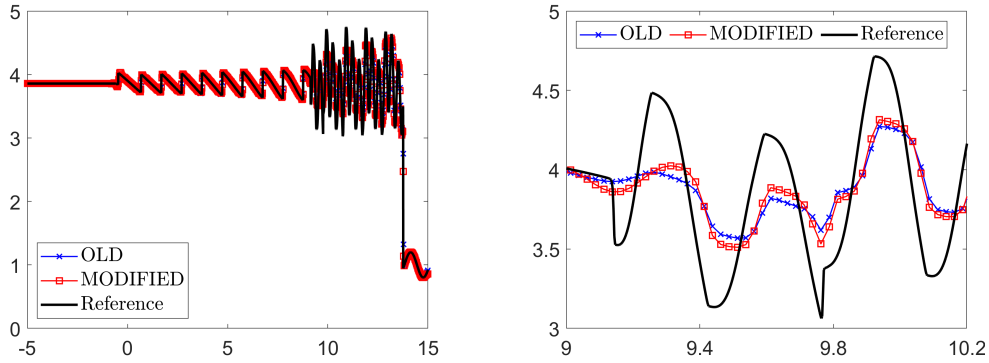


Figure 2.1: Density ρ computed with $\Delta x = 1/40$ by the OLD and MODIFIED schemes (left) and zoom at $x \in [9, 10.2]$ (right).

We then refine the mesh to $\Delta x = 1/200$ and compute the numerical solutions until the same final time $t = 5$ by both the OLD and MODIFIED schemes. The obtained densities are presented in Figure 2.2, where one can clearly see that there are “stair-like” structures in the numerical solution computed by the MODIFIED scheme; see Figure 2.2 (right). The appearance of these “stair-like” structures suggests that the value $C_1 = 0.004$ is too small and hence the identified “rough” areas, where the overcompressive limiter is applied, are too wide. We therefore take a larger value $C_1 = 0.1$ and repeat the same computations on the same two meshes. For this value of C_1 , no “stair-like” structures are formed even when the mesh is refined. However, the obtained densities, plotted in Figure 2.3, contain oscillations in the coarse mesh solution (see the top right panel in Figure 2.3). This suggests that now the identified smooth area is too wide and the quasi-linear fifth-order scheme is used near the shock waves. It is noticeable that the magnitude of oscillations near the shocks does not decay when the mesh is refined; see the bottom right panel in Figure 2.3.

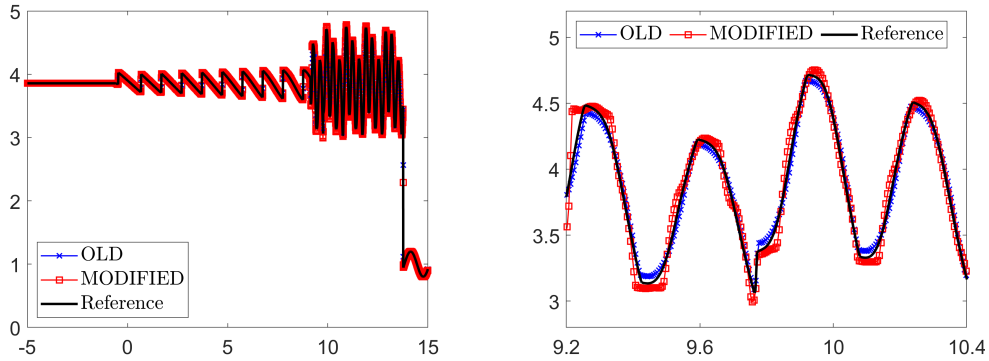


Figure 2.2: Density ρ computed with $\Delta x = 1/200$ by the OLD and MODIFIED schemes (left) and zoom at $x \in [9.2, 10.4]$ (right).

3 Novel 1-D Adaptive Schemes

In this section, we propose novel 1-D adaptive schemes, which achieve higher resolution than the adaptive schemes from [8] and at the same time do not suffer from the occurrence of either “stair-like” structures or large spurious oscillations. To this end, we first compute the pressure-based SI, which is calculated

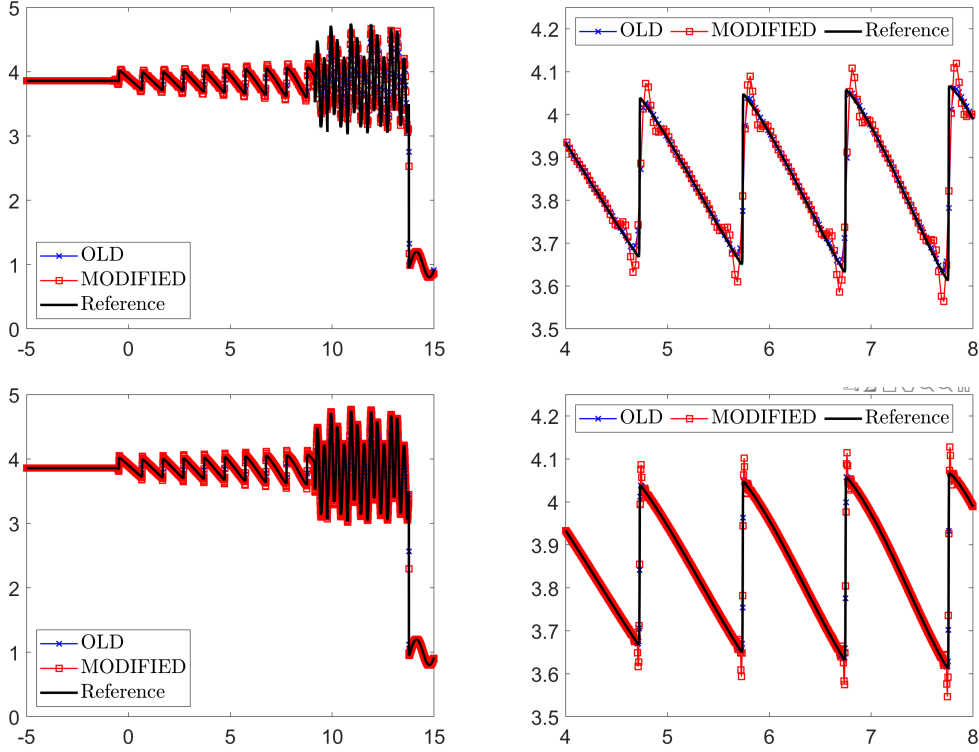


Figure 2.3: Density ρ computed with $\Delta x = 1/40$ (top row) and $\Delta x = 1/200$ (bottom row) by the OLD and MODIFIED schemes (left) and zoom at $x \in [4, 8]$ (right).

using the following quantities, which are similar to (2.5)–(2.6):

$$\mathcal{E}_j^p = \frac{|p_{j+1} - 2p_j + p_{j-1}|}{|p_{j+1} - p_j| + |p_j - p_{j-1}| + \varepsilon(p_{j+1} + 2p_j + p_{j-1})}, \quad \bar{\mathcal{E}}_j^p = \frac{1}{6}[\mathcal{E}_{j+1}^p + 4\mathcal{E}_j^p + \mathcal{E}_{j-1}^p].$$

We then take advantage of the fact at the contact discontinuities $\bar{\mathcal{E}}_j^p$ is large, but $\bar{\mathcal{E}}_j^p$ is small and design the following strategy to distinguish the neighborhoods of contact discontinuities from the other parts of “rough” areas:

- Select a tunable constant $0 < C_1 < 1$ and mark the cells I_j , in which $\bar{\mathcal{E}}_j^p > C_1$, as “rough” cells;
- Select a constant $0 < C_2 < 1$ and mark those “rough” cells I_j , in which $\bar{\mathcal{E}}_j^p < C_2$, as “contact” cells.

After identifying three different parts of the computed solution, we design a novel scheme adaption approach as follows:

Area A (neighborhoods of the contact discontinuities): Use the second-order LDCU scheme (§2.1) with the overcompressive SBM limiter (Appendix A) with $\tau = -0.25$ in (A.3);

Area B (the rest of the “rough” parts of the computed solution): Use the second-order LDCU scheme (§2.1) with the Minmod2 limiter, which is, in fact, a dissipative SBM limiter (Appendix A) with $\tau = 0.5$ in (A.3);

Area C (smooth parts of the computed solution): Use the quasi-linear fifth-order scheme (§2.2).

4 Novel 2-D Adaptive Scheme

In this section, we extend the novel 1-D adaptive strategy introduced in §3 to the 2-D case.

4.1 2-D Low-Dissipation Central-Upwind (LDCU) Schemes

In this section, we briefly review the second-order semi-discrete 2-D LDCU schemes introduced in [10].

We assume that the computational domain is covered with uniform cells $I_{j,k} := [x_{j-\frac{1}{2}}, x_{j+\frac{1}{2}}] \times [y_{k-\frac{1}{2}}, y_{k+\frac{1}{2}}]$ with $x_{j+\frac{1}{2}} - x_{j-\frac{1}{2}} \equiv \Delta x$ and $y_{k+\frac{1}{2}} - y_{k-\frac{1}{2}} \equiv \Delta y$ centered at (x_j, y_k) with $x_j = (x_{j-\frac{1}{2}} + x_{j+\frac{1}{2}})/2$ and $y_k = (y_{k-\frac{1}{2}} + y_{k+\frac{1}{2}})/2$, and that the cell averages

$$\bar{\mathbf{U}}_{j,k} := \frac{1}{\Delta x \Delta y} \iint_{I_{j,k}} \mathbf{U}(x, y, t) dx dy$$

are available at a certain time $t \geq 0$.

According to [10], $\bar{\mathbf{U}}_{j,k}$ are evolved in time by numerically solving the following system of ODEs:

$$\frac{d\bar{\mathbf{U}}_{j,k}}{dt} = -\frac{\mathcal{F}_{j+\frac{1}{2},k}[\mathbf{U}] - \mathcal{F}_{j-\frac{1}{2},k}[\mathbf{U}]}{\Delta x} - \frac{\mathcal{G}_{j,k+\frac{1}{2}}[\mathbf{U}] - \mathcal{G}_{j,k-\frac{1}{2}}[\mathbf{U}]}{\Delta y}, \quad (4.1)$$

where $\mathcal{F}_{j+\frac{1}{2},k}[\mathbf{U}]$ and $\mathcal{G}_{j,k+\frac{1}{2}}[\mathbf{U}]$ are the x - and y -directional LDCU numerical fluxes given by

$$\begin{aligned} \mathcal{F}_{j+\frac{1}{2},k}[\mathbf{U}] &= \frac{a_{j+\frac{1}{2},k}^+ \mathbf{F}(\mathbf{U}_{j+\frac{1}{2},k}^-) - a_{j+\frac{1}{2},k}^- \mathbf{F}(\mathbf{U}_{j+\frac{1}{2},k}^+)}{a_{j+\frac{1}{2},k}^+ - a_{j+\frac{1}{2},k}^-} + \frac{a_{j+\frac{1}{2},k}^+ a_{j+\frac{1}{2},k}^-}{a_{j+\frac{1}{2},k}^+ - a_{j+\frac{1}{2},k}^-} (\mathbf{U}_{j+\frac{1}{2},k}^+ - \mathbf{U}_{j+\frac{1}{2},k}^-) + \mathbf{q}_{j+\frac{1}{2},k}^x, \\ \mathcal{G}_{j,k+\frac{1}{2}}[\mathbf{U}] &= \frac{b_{j,k+\frac{1}{2}}^+ \mathbf{G}(\mathbf{U}_{j,k+\frac{1}{2}}^-) - b_{j,k+\frac{1}{2}}^- \mathbf{G}(\mathbf{U}_{j,k+\frac{1}{2}}^+)}{b_{j,k+\frac{1}{2}}^+ - b_{j,k+\frac{1}{2}}^-} + \frac{b_{j,k+\frac{1}{2}}^+ b_{j,k+\frac{1}{2}}^-}{b_{j,k+\frac{1}{2}}^+ - b_{j,k+\frac{1}{2}}^-} (\mathbf{U}_{j,k+\frac{1}{2}}^- - \mathbf{U}_{j,k+\frac{1}{2}}^+) + \mathbf{q}_{j,k+\frac{1}{2}}^y. \end{aligned}$$

Here:

- $\mathbf{U}_{j+\frac{1}{2},k}^\pm$ and $\mathbf{U}_{j,k+\frac{1}{2}}^\pm$ are the one-sided point values of \mathbf{U} at the midpoints of the cell interfaces $(x_{j+\frac{1}{2}}, y_k)$ and $(x_j, y_{k+\frac{1}{2}})$, respectively. As in the 1-D case, these one-sided point values are reconstructed out of the given set of cell averages $\{\bar{\mathbf{U}}_{j,k}\}$ using a proper nonlinear limiter; see Appendix B;
- $a_{j+\frac{1}{2},k}^\pm$ and $b_{j,k+\frac{1}{2}}^\pm$ are the one-sided local speeds of propagation in the x - and y -directions, respectively. They can be estimated using the largest and smallest eigenvalues of the corresponding Jacobians $A(\mathbf{U}) := \frac{\partial \mathbf{F}}{\partial \mathbf{U}}(\mathbf{U})$ and $B(\mathbf{U}) := \frac{\partial \mathbf{G}}{\partial \mathbf{U}}(\mathbf{U})$;
- $\mathbf{q}_{j+\frac{1}{2},k}^x$ and $\mathbf{q}_{j,k+\frac{1}{2}}^y$ are “built-in” anti-diffusion terms, which need to be derived for a particular system (1.2) at hand.

As in the 1-D case, we focus on the Euler equations of gas dynamics, whose 2-D version reads as (1.2) with

$$\mathbf{U} = (\rho, \rho u, \rho v, E)^\top, \quad \mathbf{F} = (\rho u, \rho u^2 + p, \rho uv, u(E + p))^\top, \quad \mathbf{G} = (\rho v, \rho uv, \rho v^2 + p, v(E + p))^\top. \quad (4.2)$$

Here, v is the y -velocity and the other variables are the same as in the 1-D case. The system (1.2), (4.2) is closed through the following EOS for ideal gases:

$$p = (\gamma - 1) \left[E - \frac{\rho}{2} (u^2 + v^2) \right]. \quad (4.3)$$

For the Euler system (1.1), (4.2)–(4.3), the one-sided local speeds of propagation can be estimated by

$$\begin{aligned} a_{j+\frac{1}{2},k}^+ &= \max \left\{ u_{j+\frac{1}{2},k}^+ + c_{j+\frac{1}{2},k}^+, u_{j+\frac{1}{2},k}^- + c_{j+\frac{1}{2},k}^-, 0 \right\}, \quad a_{j+\frac{1}{2},k}^- = \min \left\{ u_{j+\frac{1}{2},k}^+ - c_{j+\frac{1}{2},k}^+, u_{j+\frac{1}{2},k}^- - c_{j+\frac{1}{2},k}^-, 0 \right\}, \\ b_{j,k+\frac{1}{2}}^+ &= \max \left\{ v_{j,k+\frac{1}{2}}^+ + c_{j,k+\frac{1}{2}}^+, v_{j,k+\frac{1}{2}}^- + c_{j,k+\frac{1}{2}}^-, 0 \right\}, \quad b_{j,k+\frac{1}{2}}^- = \min \left\{ v_{j,k+\frac{1}{2}}^+ - c_{j,k+\frac{1}{2}}^+, v_{j,k+\frac{1}{2}}^- - c_{j,k+\frac{1}{2}}^-, 0 \right\}, \end{aligned}$$

where

$$\begin{aligned} u_{j+\frac{1}{2},k}^{\pm} &= \frac{(\rho u)_{j+\frac{1}{2},k}^{\pm}}{\rho_{j+\frac{1}{2},k}^{\pm}}, \quad u_{j,k+\frac{1}{2}}^{\pm} = \frac{(\rho u)_{j,k+\frac{1}{2}}^{\pm}}{\rho_{j,k+\frac{1}{2}}^{\pm}}, \quad v_{j+\frac{1}{2},k}^{\pm} = \frac{(\rho v)_{j+\frac{1}{2},k}^{\pm}}{\rho_{j+\frac{1}{2},k}^{\pm}}, \quad v_{j,k+\frac{1}{2}}^{\pm} = \frac{(\rho v)_{j,k+\frac{1}{2}}^{\pm}}{\rho_{j,k+\frac{1}{2}}^{\pm}}, \\ p_{j+\frac{1}{2},k}^{\pm} &= (\gamma - 1) \left[E_{j+\frac{1}{2},k}^{\pm} - \frac{1}{2} \rho_{j+\frac{1}{2},k}^{\pm} \left((u_{j+\frac{1}{2},k}^{\pm})^2 + (v_{j+\frac{1}{2},k}^{\pm})^2 \right) \right], \quad c_{j+\frac{1}{2},k}^{\pm} = \sqrt{\frac{\gamma p_{j+\frac{1}{2},k}^{\pm}}{\rho_{j+\frac{1}{2},k}^{\pm}}}, \\ p_{j,k+\frac{1}{2}}^{\pm} &= (\gamma - 1) \left[E_{j,k+\frac{1}{2}}^{\pm} - \frac{1}{2} \rho_{j,k+\frac{1}{2}}^{\pm} \left((u_{j,k+\frac{1}{2}}^{\pm})^2 + (v_{j,k+\frac{1}{2}}^{\pm})^2 \right) \right], \quad c_{j,k+\frac{1}{2}}^{\pm} = \sqrt{\frac{\gamma p_{j,k+\frac{1}{2}}^{\pm}}{\rho_{j,k+\frac{1}{2}}^{\pm}}}. \end{aligned}$$

Finally, a description of the anti-diffusion terms $\mathbf{q}_{j+\frac{1}{2},k}^x$ and $\mathbf{q}_{j,k+\frac{1}{2}}^y$ can be found in [10], and here, we omit the details for the sake of brevity.

As in the 1-D case, we numerically integrate the ODE system (4.1) using the three-stage third-order SSP Runge-Kutta method:

$$\begin{aligned} \mathbf{U}_{j,k}^I &= \mathbf{U}_{j,k}(t) - \frac{\Delta t}{\Delta x} \left(\mathcal{F}_{j+\frac{1}{2},k}[\mathbf{U}(t)] - \mathcal{F}_{j-\frac{1}{2},k}[\mathbf{U}(t)] \right) - \frac{\Delta t}{\Delta y} \left(\mathcal{G}_{j,k+\frac{1}{2}}[\mathbf{U}(t)] - \mathcal{G}_{j,k-\frac{1}{2}}[\mathbf{U}(t)] \right), \\ \mathbf{U}_{j,k}^{II} &= \frac{3}{4} \mathbf{U}_{j,k}(t) + \frac{1}{4} \left[\mathbf{U}_{j,k}^I - \frac{\Delta t}{\Delta x} \left(\mathcal{F}_{j+\frac{1}{2},k}[\mathbf{U}^I] - \mathcal{F}_{j-\frac{1}{2},k}[\mathbf{U}^I] \right) \right. \\ &\quad \left. - \frac{\Delta t}{\Delta y} \left(\mathcal{G}_{j,k+\frac{1}{2}}[\mathbf{U}^I] - \mathcal{G}_{j,k-\frac{1}{2}}[\mathbf{U}^I] \right) \right], \\ \mathbf{U}_{j,k}(t + \Delta t) &= \frac{1}{3} \mathbf{U}_{j,k}(t) + \frac{2}{3} \left[\mathbf{U}_{j,k}^{II} - \frac{\Delta t}{\Delta x} \left(\mathcal{F}_{j+\frac{1}{2},k}[\mathbf{U}^{II}] - \mathcal{F}_{j-\frac{1}{2},k}[\mathbf{U}^{II}] \right) \right. \\ &\quad \left. - \frac{\Delta t}{\Delta y} \left(\mathcal{G}_{j,k+\frac{1}{2}}[\mathbf{U}^{II}] - \mathcal{G}_{j,k-\frac{1}{2}}[\mathbf{U}^{II}] \right) \right]. \end{aligned} \tag{4.4}$$

In (4.4), the time step Δt is selected adaptively based on the following CFL-based stability restriction:

$$\Delta t \leq \min \left\{ \frac{\Delta x}{2a}, \frac{\Delta y}{2b} \right\}, \quad a := \max_{j,k} \left\{ \max(a_{j+\frac{1}{2},k}^+, -a_{j+\frac{1}{2},k}^-) \right\}, \quad b := \max_{j,k} \left\{ \max(b_{j,k+\frac{1}{2}}^+, -b_{j,k+\frac{1}{2}}^-) \right\}.$$

As in the 1-D case, we have replaced in (4.4) the cell averages of \mathbf{U} with its point values ($\mathbf{U}_{j,k}(t) \approx \mathbf{U}(x_j, y_k, t^n)$). This does not affect the accuracy of the second-order scheme as the difference between the cell averages and point values is proportional to $\mathcal{O}((\Delta x)^2 + \mathcal{O}((\Delta y)^2)$ for smooth solutions.

4.2 2-D Quasi-Linear Fifth-Order Scheme

In this section, we extend the 1-D quasi-linear fifth-order scheme described in §2.2 to the 2-D case. The extension is performed in a “dimension-by-dimension” manner.

Assuming the point values $\mathbf{U}_{j,k}$ are available at a certain time level t , the solution is evolved to the next time level $t + \Delta t$ according to (4.4) with the following numerical fluxes:

$$\begin{aligned} \mathcal{F}_{j+\frac{1}{2},k}[\mathbf{U}(t)] &= \mathcal{L}_{j+\frac{1}{2},k}^x[\mathbf{U}(t)], \quad \mathcal{F}_{j+\frac{1}{2},k}[\mathbf{U}^I] = \mathcal{L}_{j+\frac{1}{2},k}^x[\mathbf{U}^I], \quad \mathcal{F}_{j+\frac{1}{2},k}[\mathbf{U}^{II}] = \mathcal{L}_{j+\frac{1}{2},k}^x[\mathbf{U}^{II}] - \boldsymbol{\omega}_{j+\frac{1}{2},k}^x(t), \\ \mathcal{G}_{j,k+\frac{1}{2}}[\mathbf{U}(t)] &= \mathcal{L}_{j,k+\frac{1}{2}}^y[\mathbf{U}(t)], \quad \mathcal{G}_{j,k+\frac{1}{2}}[\mathbf{U}^I] = \mathcal{L}_{j,k+\frac{1}{2}}^y[\mathbf{U}^I], \quad \mathcal{G}_{j,k+\frac{1}{2}}[\mathbf{U}^{II}] = \mathcal{L}_{j,k+\frac{1}{2}}^y[\mathbf{U}^{II}] - \boldsymbol{\omega}_{j,k+\frac{1}{2}}^y(t), \end{aligned}$$

where

$$\begin{aligned}\mathcal{L}_{j+\frac{1}{2},k}^x[\mathbf{U}] &:= \frac{1}{60} [\mathbf{F}(\mathbf{U}_{j+3,k}) - 8\mathbf{F}(\mathbf{U}_{j+2,k}) + 37\mathbf{F}(\mathbf{U}_{j+1,k}) + 37\mathbf{F}(\mathbf{U}_{j,k}) - 8\mathbf{F}(\mathbf{U}_{j-1,k}) + \mathbf{F}(\mathbf{U}_{j-2,k})], \\ \boldsymbol{\omega}_{j+\frac{1}{2},k}^x(t) &:= \frac{3\Delta x}{128\Delta t} [\mathbf{U}_{j+3,k}(t) - 5\mathbf{U}_{j+2,k}(t) + 10\mathbf{U}_{j+1,k}(t) - 10\mathbf{U}_{j,k}(t) + 5\mathbf{U}_{j-1,k}(t) - \mathbf{U}_{j-2,k}(t)], \\ \mathcal{L}_{j,k+\frac{1}{2}}^y[\mathbf{U}] &:= \frac{1}{60} [\mathbf{G}(\mathbf{U}_{j,k+3}) - 8\mathbf{G}(\mathbf{U}_{j,k+2}) + 37\mathbf{G}(\mathbf{U}_{j,k+1}) + 37\mathbf{G}(\mathbf{U}_{j,k}) - 8\mathbf{G}(\mathbf{U}_{j,k-1}) + \mathbf{G}(\mathbf{U}_{j,k-2})], \\ \boldsymbol{\omega}_{j,k+\frac{1}{2}}^y(t) &:= \frac{3\Delta y}{128\Delta t} [\mathbf{U}_{j,k+3}(t) - 5\mathbf{U}_{j,k+2}(t) + 10\mathbf{U}_{j,k+1}(t) - 10\mathbf{U}_{j,k}(t) + 5\mathbf{U}_{j,k-1}(t) - \mathbf{U}_{j,k-2}(t)],\end{aligned}$$

In the next numerical example, we demonstrate that the developed 2-D quasi-linear scheme achieves the fifth order of accuracy in capturing a smooth solution.

Example—2-D Accuracy Test. We consider the following smooth initial data [3, 38]:

$$\begin{aligned}\rho(x, y, 0) &= \left(1 - \frac{(\gamma - 1)\kappa^2}{2\gamma}\right)^{\frac{1}{\gamma-1}}, \quad p(x, y, 0) = \rho^\gamma(x, y, 0), \\ u(x, y, 0) &= 1 - \kappa y, \quad v(x, y, 0) = 1 + \kappa x, \quad \kappa = \frac{5}{2\pi} e^{\frac{1-x^2-y^2}{2}}\end{aligned}$$

subject to the periodic boundary conditions in the computational domain $[-10, 10] \times [-10, 10]$. The exact solution of this initial value problem is given by $\mathbf{U}(x, y, t) = \mathbf{U}(x - t, y - t, 0)$.

We compute the numerical solution until the final time $t = 0.1$ on a sequence of uniform meshes with $\Delta x = \Delta y = 1/100, 1/200, 1/400, 1/800$, and $1/1600$ and $\Delta t \sim \min\{(\Delta x)^{\frac{5}{3}}, (\Delta y)^{\frac{5}{3}}\}$, and then measure the L^1 -errors and the corresponding experimental convergence rates. The obtained results are presented in Table 4.1, where one can see that the expected fifth order of accuracy has been achieved.

$\Delta x = \Delta y$	ρ		u		v		p	
	Error	Rate	Error	Rate	Error	Rate	Error	Rate
1/10	3.35e-06	—	6.01e-06	—	6.33e-06	—	4.85e-06	—
1/20	1.02e-07	5.03	1.82e-07	5.04	1.97e-07	5.01	1.48e-07	5.04
1/40	3.56e-09	4.85	6.36e-09	4.84	6.89e-09	4.84	5.14e-09	4.85
1/80	1.15e-10	4.95	2.07e-10	4.94	2.24e-10	4.94	1.66e-10	4.95

Table 4.1: The L^1 -errors and experimental convergence rates for ρ , u , v , and p computed by the quasi-linear fifth-order scheme.

4.3 2-D Adaptive Algorithm

We now turn to the description of the proposed 2-D adaptive schemes.

We first introduce the quantities [8], which are similar to (2.5):

$$\begin{aligned}\mathcal{E}_{j,k}^\rho &= \sqrt{\frac{\mathcal{E}_{j,k}^{1,\rho}}{\mathcal{E}_{j,k}^{2,\rho}}}, \quad \mathcal{E}_{j,k}^{1,\rho} = (\rho_{j+1,k} - 2\rho_{j,k} + \rho_{j-1,k})^2 + (\rho_{j,k+1} - 2\rho_{j,k} + \rho_{j,k-1})^2, \\ \mathcal{E}_{j,k}^{2,\rho} &= ((|\rho_{j+1,k} - \rho_{j,k}| + |\rho_{j,k} - \rho_{j-1,k}| + \varepsilon[|\bar{\rho}_{j+1,k}| + 2|\rho_{j,k}| + |\rho_{j-1,k}|])^2 \\ &\quad + ((|\rho_{j,k+1} - \rho_{j,k}| + |\rho_{j,k} - \rho_{j,k-1}| + \varepsilon[|\rho_{j,k+1}| + 2|\rho_{j,k}| + |\rho_{j,k-1}|])^2,\end{aligned}$$

and to (2.6):

$$\bar{\mathcal{E}}_{j,k}^{\rho} = \frac{1}{36} \left[\mathcal{E}_{j-1,k-1}^{\rho} + \mathcal{E}_{j-1,k+1}^{\rho} + \mathcal{E}_{j+1,k-1}^{\rho} + \mathcal{E}_{j+1,k+1}^{\rho} + 4(\mathcal{E}_{j-1,k}^{\rho} + \mathcal{E}_{j,k-1}^{\rho} + \mathcal{E}_{j,k+1}^{\rho} + \mathcal{E}_{j+1,k}^{\rho}) + 16\mathcal{E}_{j,k}^{\rho} \right].$$

The values of $\mathcal{E}_{j,k}^p$ and $\bar{\mathcal{E}}_{j,k}^p$ can be computed in a same manner by replacing ρ with p .

Equipped with $\bar{\mathcal{E}}_{j,k}^{\rho}$ and $\bar{\mathcal{E}}_{j,k}^p$, we proceed as in the 1-D case:

As in the 1-D case, we use an overcompressive SBM limiter in the contact wave regions of the computed solution, the Minmod2 limiter in the shock wave regions, and the fifth-order scheme in the rest parts. To this end, we detect the smoothness of the numerical solution using the 2-D version of the SI proposed in [30]:

- Select a tunable constant $0 < C_1 < 1$ and mark the cells $I_{j,k}$, in which $\bar{\mathcal{E}}_{j,k}^{\rho} > C_1$, as “rough” cells;
- Select a constant $0 < C_2 < 1$ and mark those “rough” cells $I_{j,k}$, in which $\bar{\mathcal{E}}_{j,k}^p < C_2$, as “contact” cells.

After identifying three different parts of the computed solution, we design a 2-D scheme adaption algorithm as follows:

Area A (neighborhoods of the contact discontinuities): Use the second-order LDCU scheme (§4.1) with the overcompressive SBM limiter (Appendix B) with $\tau = -0.25$ in (A.3);

Area B (the rest of the “rough” parts of the computed solution): Use the second-order LDCU scheme (§4.1) with the Minmod2 limiter, which is, in fact, a dissipative SBM limiter (Appendix B) with $\tau = 0.5$ in (A.3);

Area C (smooth parts of the computed solution): Use the quasi-linear fifth-order scheme (§4.2).

5 Numerical Examples

In this section, we apply the developed adaptive schemes to both the 1-D and 2-D Euler equations of gas dynamics and compare the performance the adaptive schemes from [8] (OLD schemes) and novel adaptive schemes, which will be referred to as NEW schemes. We take $\gamma = 1.4$ in Examples 1–7 and $\gamma = 5/3$ in Example 8. In all of the examples, we use the CFL number 0.4.

All of the numerical experiments have been conducted on a workstation equipped with an Intel(R) Core(TM) i7-9750H CPU at 2.6 GHz and 32 GB of RAM. The simulations were conducted in FORTRAN using GCC version 14.2.0 compiler suite. The reported CPU times were averaged over thirty independent runs to ensure reproducibility and minimize variability due to system processes.

5.1 1-D Examples

In the 1-D examples, the adaptive solutions will be plotted along with the reference solutions, which will be computed using the second-order LDCU scheme described in §2.1 and implemented with the Minmod2 limiter.

Example 1—Shock-Density Wave Interaction Problem. In the first example, we reconsider the example from §2.3. We compute the numerical solutions by the NEW (with the adaption constants $C_1 = 0.015$ and $C_2 = 0.15$) and OLD (with the adaption constant $C_1 = 0.01$) schemes on uniform meshes with $\Delta x = 1/40$ and $1/200$ until the final time $t = 5$. We present the obtained numerical results in Figure 5.1 together with the reference solution computed on a much finer mesh with $\Delta x = 1/400$. One can see that, compared with the OLD scheme, the NEW one produces a slightly more accurate result; see Figure 5.1 (right). At the same time, there are neither oscillations near the shocks (see Figure 5.2 (left)) nor “stair-like” structures in the smooth parts of the computed solution (see Figure 5.2 (right)), when a finer mesh with $\Delta x = 1/200$ is used; compare these results with those reported in Figures 2.2 and 2.3.

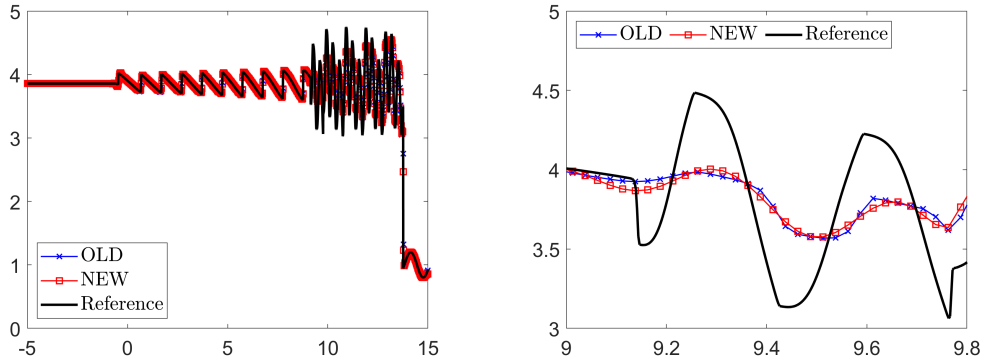


Figure 5.1: Example 1: Density ρ computed on a uniform mesh with $\Delta x = 1/40$ by the NEW and OLD schemes (left) and zoom at $x \in [9, 9.8]$ (right).

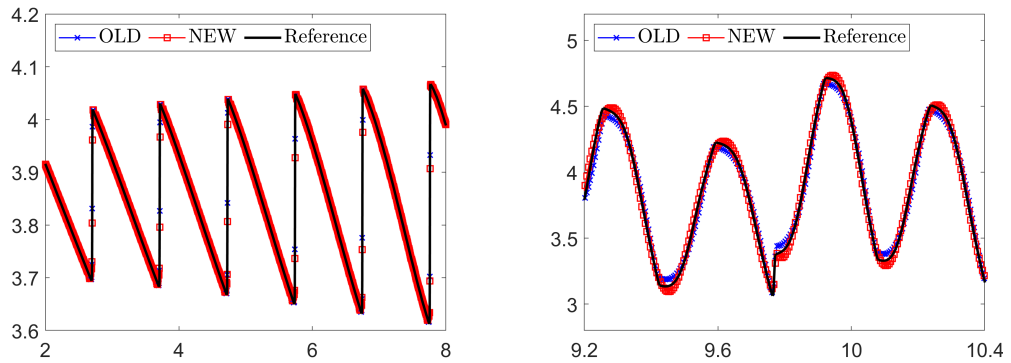


Figure 5.2: Example 1: Density ρ computed on a uniform mesh with $\Delta x = 1/200$ by the NEW and OLD schemes—zoom at $x \in [4, 8]$ (left) and $x \in [9.2, 10.4]$ (right).

We then measure the CPU times consumed by both of the studied schemes on a uniform mesh with $\Delta x = 1/4000$ and the CPU time consumed by the OLD scheme is about 356% larger than the CPU time consumed by the NEW scheme. This demonstrates that the NEW scheme is not only more accurate, but also substantially more efficient than its OLD counterpart. We stress that the NEW scheme is highly efficient due to an extremely low computational cost of the quasi-linear fifth-order scheme.

Example 2—Shock-Entropy Wave Interaction Problem. In the second example taken from [40], we consider the shock-entropy wave interaction problem with the following initial conditions:

$$(\rho, u, p) \Big|_{(x,0)} = \begin{cases} (1.51695, 0.523346, 1.805), & x < -4.5, \\ (1 + 0.1 \sin(20x), 0, 1), & x > -4.5, \end{cases}$$

which correspond to a forward-facing shock wave of Mach number 1.1 interacting with high-frequency density perturbations, that is, as the shock wave moves, the perturbations spread ahead. We set the free boundary condition at the both ends of the computational domain $[-5, 5]$.

We compute the numerical solution until the final time $t = 5$ by the NEW (with the adaption constants $C_1 = 0.02$ and $C_2 = 0.3$) and OLD (with the adaption constant $C_1 = 0.01$) schemes on a uniform mesh with $\Delta x = 1/60$. The obtained numerical results are presented in Figure 5.3 along with the reference solution computed on a much finer mesh with $\Delta x = 1/1600$, where one can see that the NEW scheme is substantially more accurate than the OLD one.

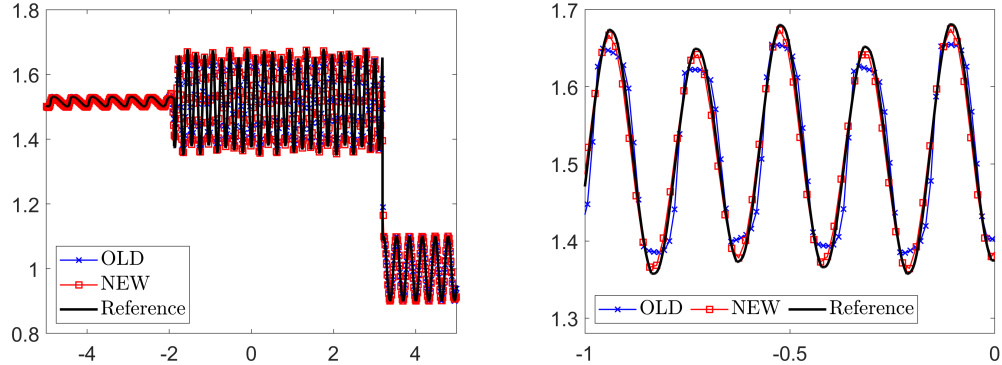


Figure 5.3: Example 2: Density ρ computed by the NEW and OLD schemes (left) and zoom at $x \in [-1, 0]$ (right).

Example 3—Blast Wave Problem. In the last 1-D example, we consider a strong shocks interaction problem from [46] with the initial data,

$$(\rho, u, p) \Big|_{(x, 0)} = \begin{cases} (1, 0, 1000), & x < 0.1, \\ (1, 0, 0.01), & 0.1 \leq x \leq 0.9, \\ (1, 0, 100), & x > 0.9, \end{cases}$$

prescribed in the computational domain $[0, 1]$ subject to the solid wall boundary conditions.

We compute the numerical solutions until the final time $t = 0.038$ by the NEW (with the adaption constants $C_1 = 0.02$ and $C_2 = 0.3$) and OLD (with the adaption constant $C_1 = 0.01$) schemes on a uniform mesh with $\Delta x = 1/400$ and present the obtained numerical results in Figure 5.4 together with the reference solution computed on a much finer mesh with $\Delta x = 1/4000$. It can be observed that both the NEW and OLD schemes are capable of achieving a superb resolution of the contact wave located at about $x = 0.6$.

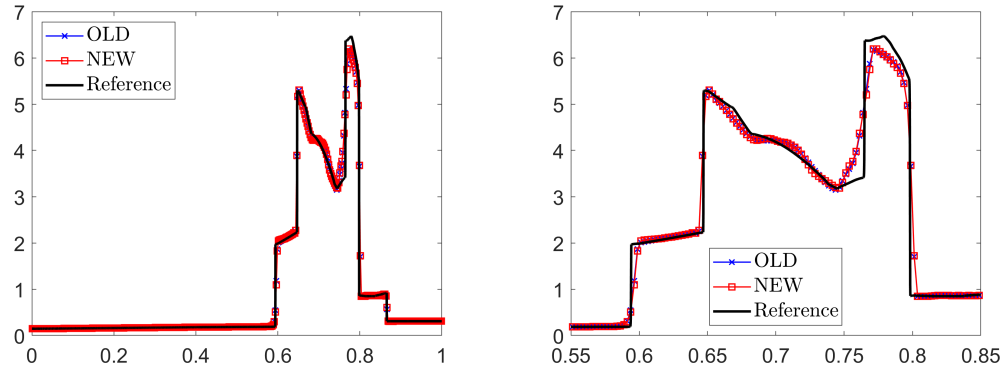


Figure 5.4: Example 3: Density ρ computed by the NEW and OLD schemes (left) and zoom at $x \in [0.55, 0.85]$.

5.2 2-D Examples

We now turn to the 2-D numerical examples. In Examples 4–6, we will consider three different 2-D Riemann problems from [25]; see also [35, 36, 47].

In all of the examples below, we will show the computed densities and the corresponding “rough” areas detected by the SIs. In the plots obtained by the NEW scheme, we also highlight in red color the detected “contact” subareas of the “rough” areas.

Example 4—2-D Riemann Problem (Configuration 3). In this example, the initial conditions,

$$(\rho, u, v, p) \Big|_{(x,y,0)} = \begin{cases} (1.5, 0, 0, 1.5), & x > 1, y > 1, \\ (0.5323, 1.206, 0, 0.3), & x < 1, y > 1, \\ (0.138, 1.206, 1.206, 0.029), & x < 1, y < 1, \\ (0.5323, 0, 1.206, 0.3), & x > 1, y < 1, \end{cases}$$

are prescribed in the computational domain $[0, 1.2] \times [0, 1.2]$ subject to the free boundary conditions.

We compute the numerical solution until the final time $t = 1$ by the NEW (with the adaption constants $C_1 = 0.08$ and $C_2 = 0.2$) and OLD (with the adaption constant $C_1 = 0.08$) schemes on a uniform mesh with $\Delta x = \Delta y = 3/2500$. The obtained results are plotted in Figure 5.5, where one can see that the NEW scheme slightly outperforms the OLD one in capturing a sideband instability of the jet in the zones of strong along-jet velocity shear and the instability along the jets neck. In Figure 5.6, we show the detected “rough” areas (for both the NEW and OLD schemes) and their “contact” subareas (for the NEW scheme). As one can see, when the NEW scheme is used, the SBM and Minmod2 limiters are implemented only in a small part of the computational domain.

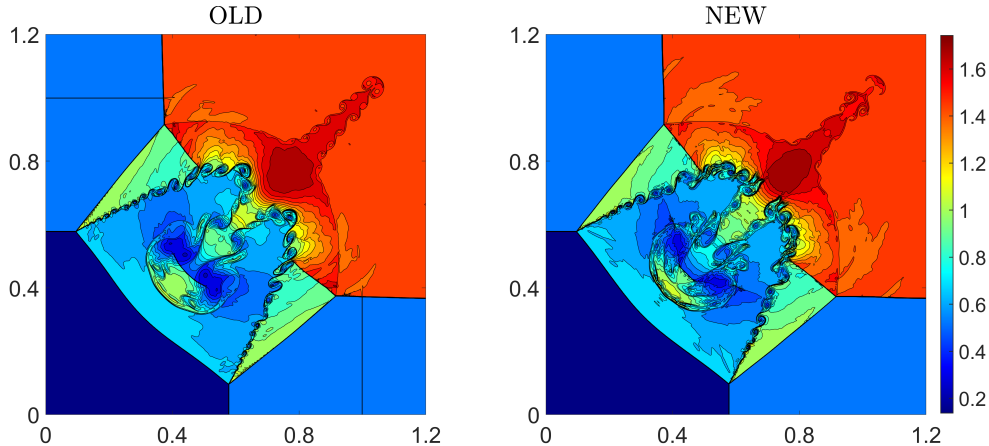


Figure 5.5: Example 4: Density ρ computed by the OLD (left) and NEW (right) schemes.

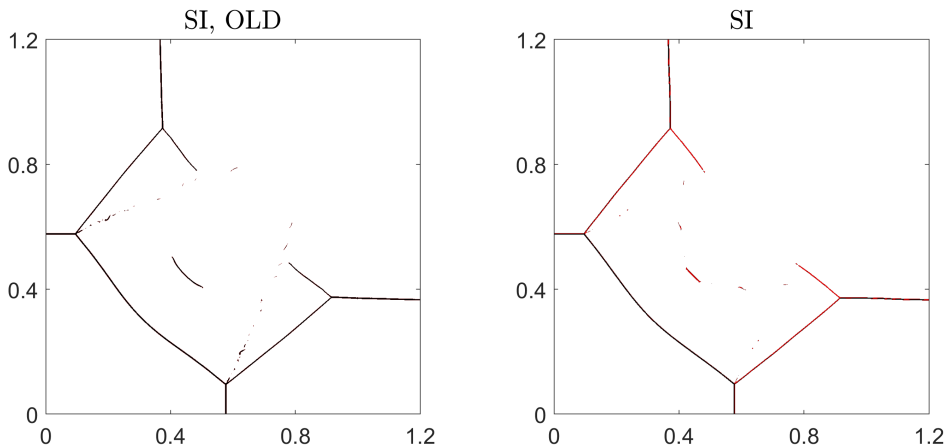


Figure 5.6: Example 4: The “rough” areas detected by the OLD (left) and NEW (right) schemes at the final time-step.

Example 5—2-D Riemann Problem (Configuration 6). In this example, the initial conditions,

$$(\rho, u, v, p) \Big|_{(x,y,0)} = \begin{cases} (1, 0.75, -0.5, 1), & x > 0.5, y > 0.5, \\ (2, 0.75, 0.5, 1), & x < 0.5, y > 0.5, \\ (1, -0.75, 0.5, 1), & x < 0.5, y < 0.5, \\ (3, -0.75, -0.5, 1), & x > 0.5, y < 0.5, \end{cases}$$

are prescribed in the computational domain $[0, 1] \times [0, 1]$ subject to the free boundary conditions.

We compute the numerical solution until the final time $t = 1$ by the second-order LDCU (implemented with the Minmod2 limiter), NEW (with the adaption constants $C_1 = 0.06$ and $C_2 = 0.004$), and OLD (with the adaption constant $C_1 = 0.1$) schemes on a uniform mesh with $\Delta x = \Delta y = 1/600$, and plot the obtained results in Figure 5.7, where one can see that the adaptive schemes clearly outperform the LDCU one. At the same time, the NEW scheme is capable of capturing much more complicated vortex structures compared with the OLD scheme, which demonstrates higher resolution and lower numerical dissipation of the NEW scheme. Note that the “rough” areas identified by both the NEW and OLD schemes are quite similar; see Figure 5.8.

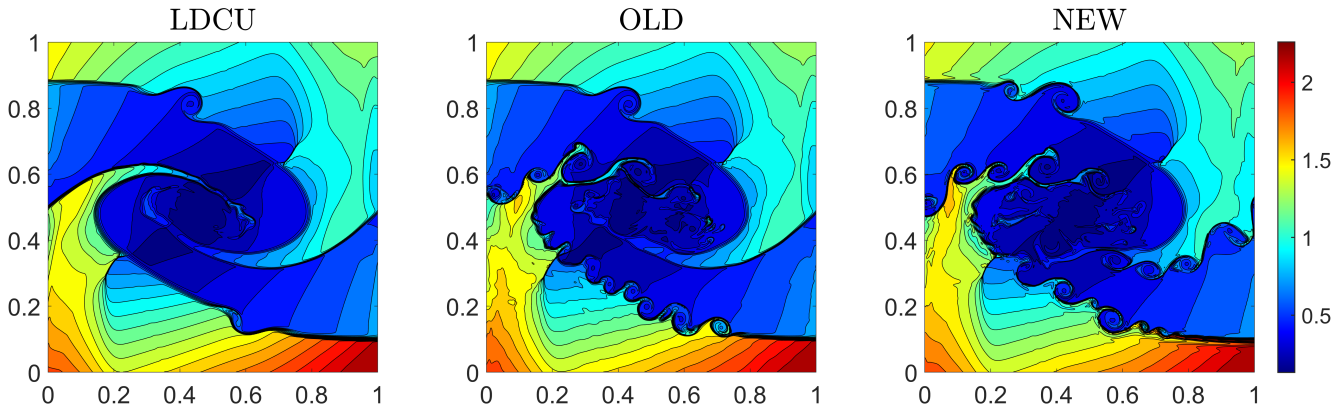


Figure 5.7: Example 5: Density ρ computed by the LDCU (left), OLD (middle), and NEW (right) schemes.

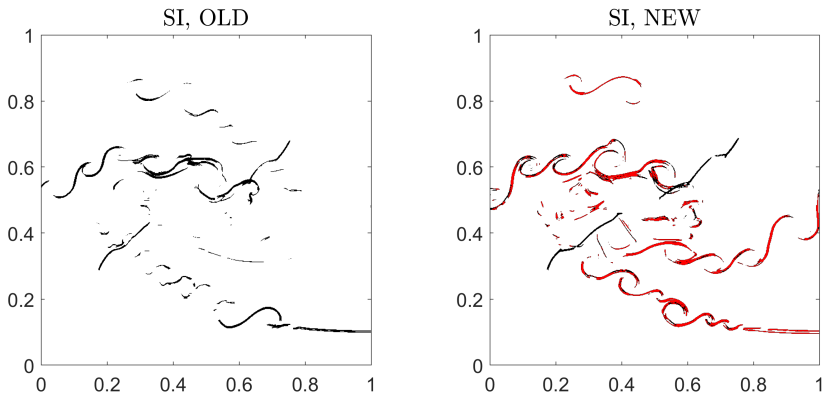


Figure 5.8: Example 5: The “rough” areas detected by the OLD (left) and NEW (right) schemes at the final time-step.

Example 6—2-D Riemann Problem (Configuration 12). In this example, the initial conditions,

$$(\rho, u, v, p) \Big|_{(x,y,0)} = \begin{cases} (0.5313, 0, 0, 0.4), & x > 0.5, y > 0.5, \\ (1, 0.7276, 0, 1), & x < 0.5, y > 0.5, \\ (0.8, 0, 0, 1), & x < 0.5, y < 0.5, \\ (1, 0, 0.7276, 1), & x > 0.5, y < 0.5, \end{cases}$$

are prescribed in the computational domain $[0, 0.6] \times [0, 0.6]$ subject to the free boundary conditions.

We compute the numerical solution until the final time $t = 0.5$ by the second-order LDCU (implemented with the Minmod2 limiter), NEW (with the adaption constants $C_1 = 0.03$ and $C_2 = 0.2$), and OLD (with the adaption constant $C_1 = 0.03$) schemes on a uniform mesh with $\Delta x = \Delta y = 1/1000$, and plot the obtained results in Figure 5.9. As one can see, the NEW scheme resolves substantially more vortices, arising along the unstable contact surfaces, than both the OLD and LDCU schemes. As in the previous examples, the “rough” areas detected by the NEW and OLD schemes are quite similar; see Figure 5.10.

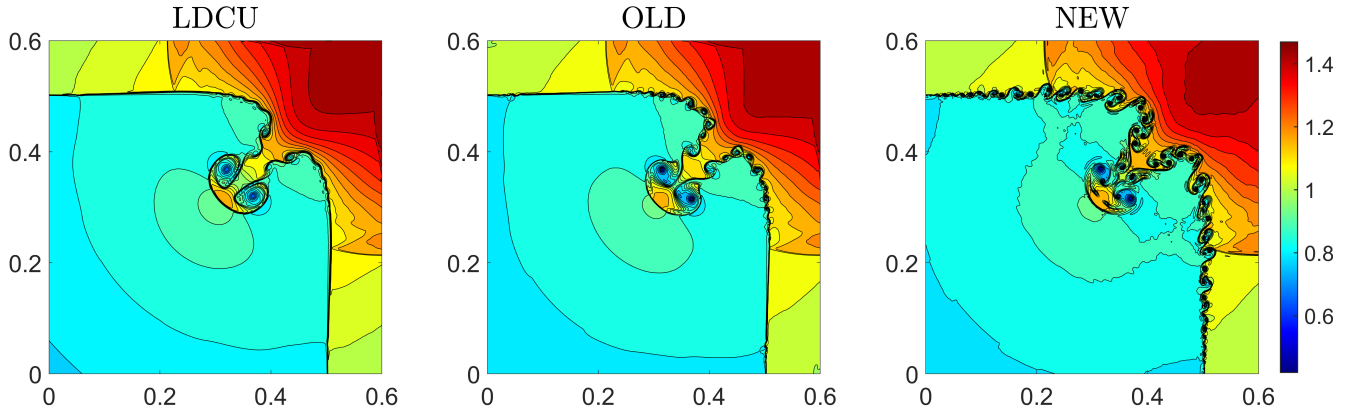


Figure 5.9: Example 6: Density ρ computed by the LDCU (left), OLD (middle), and NEW (right) schemes.

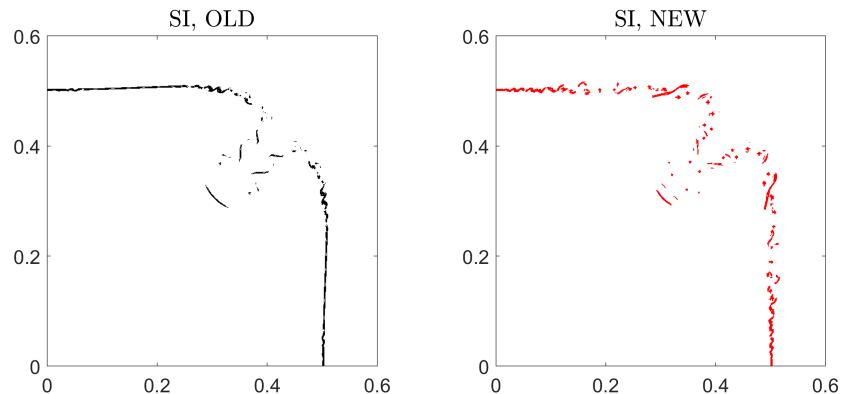


Figure 5.10: Example 6: The “rough” areas detected by the OLD (left) and NEW (right) schemes at the final time-step.

Example 7—Implosion Problem. In this example, we consider the implosion problem taken from [29]. The initial conditions,

$$(\rho, u, v, p) \Big|_{(x,y,0)} = \begin{cases} (0.125, 0, 0, 0.14), & |x| + |y| < 0.15, \\ (1, 0, 0, 1), & \text{otherwise,} \end{cases}$$

are prescribed in the computational domain $[0, 0.5] \times [0, 0.5]$ with the solid wall boundary conditions. In this setting, a jet forms near the origin and propagates along the diagonal $y = x$ direction, and the position of the jet indicates the amount of numerical dissipation present in studied numerical schemes. In general, schemes containing large numerical dissipation may not resolve the jet at all or the jet propagation velocity may be affected by the numerical diffusion.

We compute the numerical solution until the final time $t = 2.5$ by the NEW (with the adaption constants $C_1 = 0.05$ and $C_2 = 0.1$) and OLD (with the adaption constant $C_1 = 0.05$) schemes on a uniform mesh with $\Delta x = \Delta y = 1/2000$ and present the obtained numerical results in Figure 5.11. As one can observe, compared with the OLD scheme, the jet propagates much further in the diagonal direction in the numerical result computed by the NEW scheme, which demonstrates that the NEW scheme is less dissipative. In Figure 5.12, we show “rough” areas detected by the NEW and OLD schemes. One can see that when the NEW scheme is used, a sharper SBM limiter is implemented only in a very small part of the computational domain, which is substantially smaller than the one detected as “rough” by the OLD scheme.

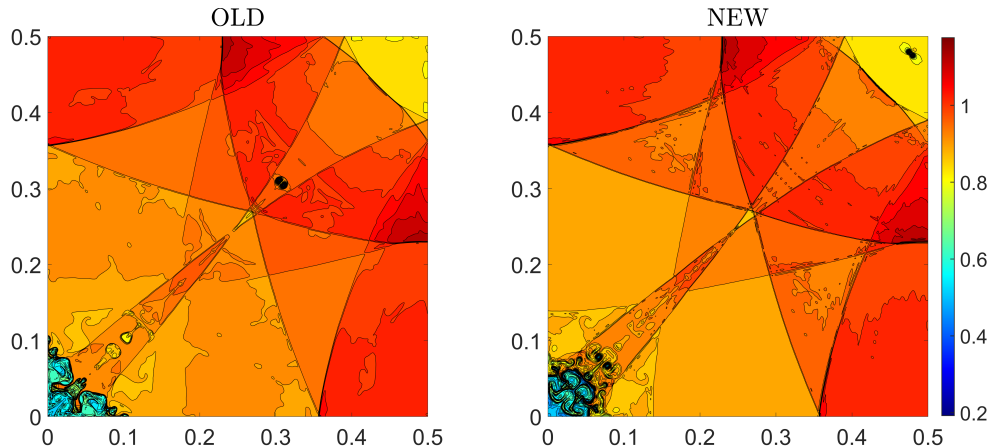


Figure 5.11: Example 7: Density ρ computed by the OLD (left) and NEW (right) schemes.

Next, we measure the CPU times consumed by the NEW and OLD schemes. The obtained results show that the CPU time consumed by the OLD scheme is about 122% larger than the CPU time consumed by the NEW scheme. This demonstrates that like in the 1-D case, the 2-D NEW scheme is substantially more efficient than the OLD one though the efficiency gain in the 2-D case is not as big as in the 1-D one (see Example 1).

Example 8—RT Instability. In the last example taken from [37], we investigate the RT instability, which is a physical phenomenon occurring when a layer of heavier fluid is placed on top of a layer of lighter fluid. To this end, we first modify the 2-D Euler equations of gas dynamics (1.2), (4.2)–(4.3) by adding the gravitational source terms acting in the positive direction of the y -axis into the RHS of the

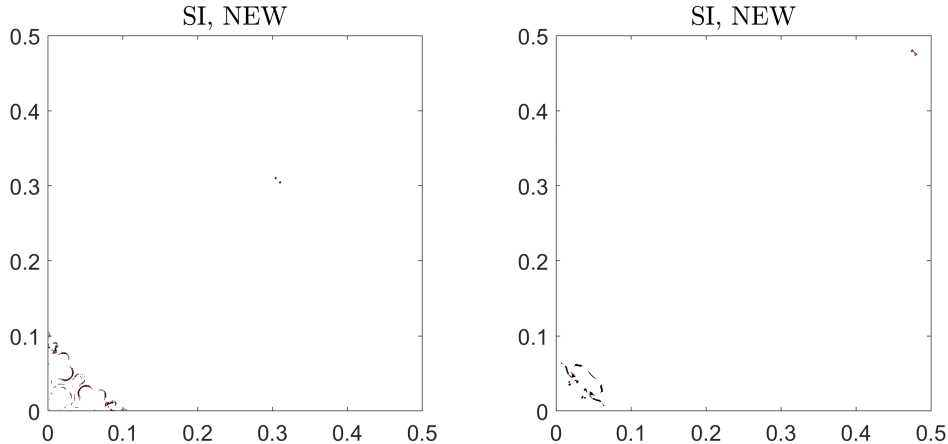


Figure 5.12: Example 7: The “rough” areas detected by the OLD (left) and NEW (right) schemes at the final time-step.

system:

$$\begin{aligned} \rho_t + (\rho u)_x + (\rho v)_y &= 0, \\ (\rho u)_t + (\rho u^2 + p)_x + (\rho uv)_y &= 0, \\ (\rho v)_t + (\rho uv)_x + (\rho v^2 + p)_y &= \rho, \\ E_t + [u(E + p)]_x + [v(E + p)]_y &= \rho v, \end{aligned}$$

and then use the following initial conditions:

$$(\rho, u, v, p) \Big|_{(x,y,0)} = \begin{cases} (2, 0, -0.025c \cos(8\pi x), 2y + 1), & y < 0.5, \\ (1, 0, -0.025c \cos(8\pi x), y + 1.5), & \text{otherwise,} \end{cases}$$

where $c := \sqrt{\gamma p / \rho}$ is the speed of sound. The solid wall boundary conditions are imposed at $x = 0$ and $x = 0.25$, and the following Dirichlet boundary conditions are specified at the top and bottom boundaries:

$$(\rho, u, v, p)(x, 1, t) = (1, 0, 0, 2.5), \quad (\rho, u, v, p)(x, 0, t) = (2, 0, 0, 1).$$

We compute the numerical solution until the final time $t = 2.95$ by the NEW (with the adaption constants $C_1 = 0.08$ and $C_2 = 0.008$) and OLD (with the adaption constant $C_1 = 0.08$) schemes on a uniform mesh with $\Delta x = \Delta y = 1/1024$ in the computational domain $[0, 0.25] \times [0, 1]$. The obtained numerical results are presented in Figure 5.13, where one can see that the NEW scheme is less dissipative than the OLD scheme. As in the previous examples, we also show the “rough” areas detected by the studied schemes; see Figure 5.14, where one can see that in the NEW scheme, the overcompressive limiter is used in smaller areas compared with the OLD scheme.

6 Conclusion

We have introduced novel adaptive schemes for hyperbolic systems of conservation laws. The new schemes are based on a scheme adaption strategy recently introduced in [8]. Like any adaptive scheme, the proposed one utilizes a smoothness indicator (SI) to automatically detect “rough” and smooth parts of the computed solution at each time-step. We then use the same SI to identify vicinities of contact discontinuities within the detected “rough” areas. In the case of Euler equations of gas dynamics, this is achieved by applying the SI to the density field, which is discontinuous at contact waves, and to the pressure, which is continuous there.

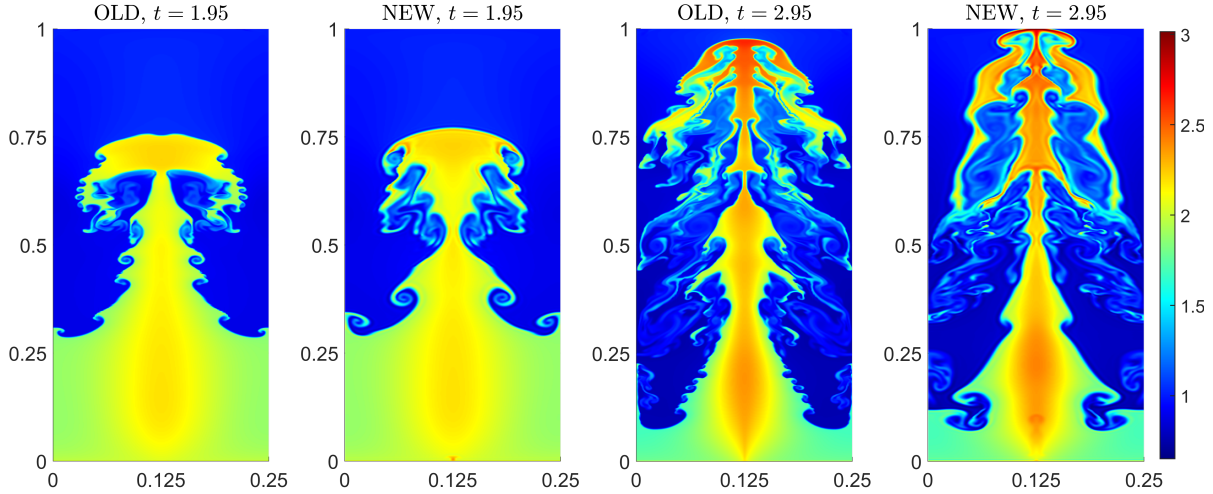


Figure 5.13: Example 8: Density ρ computed by the OLD and NEW adaptive schemes.

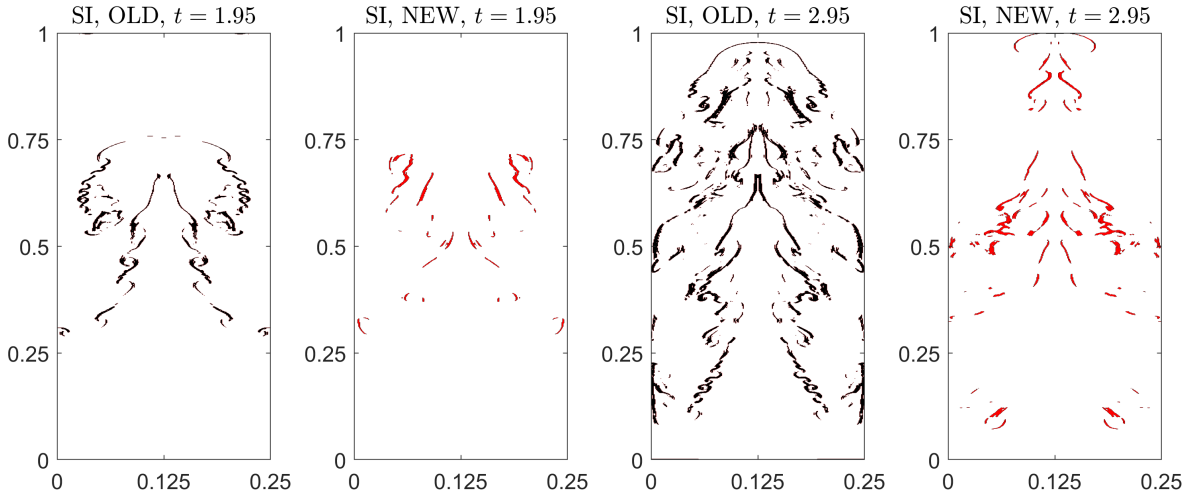


Figure 5.14: Example 8: The “rough” areas detected by the OLD (left) and NEW (right) schemes at the final time-step.

After splitting the computational domain into the corresponding three areas—“contact”, “rough”, and “smooth”—we apply different schemes inside each of them. In the “contact” areas, we use the low-dissipation central-upwind (LDCU) scheme with the overcompressive SBM limiter, which helps to extremely sharply resolve contact discontinuities. In the rest of the “rough” areas, we use the LDCU scheme with the dissipative Minmod2 limiter, which helps to both capture shock waves in a non-oscillatory manner and prevent appearance of artificial staircase-like structures, which may be developed when the overcompressive limiter is used. Finally, in the “smooth” area, we use a recently proposed very simple quasi-linear fifth-order finite-difference scheme, which helps to extremely accurately capture smooth parts of the computed solution.

The new adaptive schemes have been tested on a number of one- and two-dimensional numerical examples, which clearly demonstrate the ability of the proposed schemes to achieve very high resolution, while being robust. We also show that the new schemes clearly outperform the adaptive schemes from [8], while being substantially more efficient thanks to a very low computational cost of the quasi-linear fifth-order schemes.

Declarations:

Funding. The work of S. Chu was funded by the DFG–SPP 2183: Eigenschaftsgeregelte Umformprozesse with the Project(s) HE5386/19-2,19-3 Entwicklung eines flexiblen isothermen Reckschmiede- prozesses für die eigenschaftsgeregelte Herstellung von Turbinenschaufeln aus Hochtemperaturwerkstoffen (424334423) and by the Deutsche Forschungsgemeinschaft (DFG, German Research Foundation)–SPP 2410 Hyperbolic Balance Laws in Fluid Mechanics: Complexity, Scales, Randomness (CoScaRa) within the Project(s) HE5386/27-1 (Zufällige kompressible Euler Gleichungen: Numerik und ihre Analysis, 525853336). The work of A. Kurganov was supported in part by NSFC grants 12171226 and W2431004.

Conflicts of interest. On behalf of all authors, the corresponding author states that there is no conflict of interest.

Data and software availability. The data that support the findings of this study and FORTRAN codes developed by the authors and used to obtain all of the presented numerical results are available from the corresponding author upon reasonable request.

A 1-D LCD-Based Piecewise Linear Reconstruction

In this appendix, we briefly describe a family of SBM limiters introduced in [28], which are applied to the local characteristic variables to compute the one-sided point values $\mathbf{U}_{j+\frac{1}{2}}^\pm$. To this end, we first introduce the matrices $\widehat{\mathbf{A}}_{j+\frac{1}{2}} = \mathbf{A}(\widehat{\mathbf{U}}_{j+\frac{1}{2}})$, where $\widehat{\mathbf{U}}_{j+\frac{1}{2}} = (\overline{\mathbf{U}}_j + \overline{\mathbf{U}}_{j+1})/2$, and compute the matrices $R_{j+\frac{1}{2}}$ and $R_{j+\frac{1}{2}}^{-1}$ such that $R_{j+\frac{1}{2}}^{-1} \widehat{\mathbf{A}}_{j+\frac{1}{2}} R_{j+\frac{1}{2}}$ are diagonal. We then introduce the local characteristic variables $\boldsymbol{\Gamma}$ in the neighborhood of $x = x_{j+\frac{1}{2}}$:

$$\boldsymbol{\Gamma}_k = R_{j+\frac{1}{2}}^{-1} \overline{\mathbf{U}}_k, \quad k = j-1, j, j+1, j+2.$$

Equipped with the values $\boldsymbol{\Gamma}_{j-1}$, $\boldsymbol{\Gamma}_j$, $\boldsymbol{\Gamma}_{j+1}$, and $\boldsymbol{\Gamma}_{j+2}$, we compute the slopes

$$(\boldsymbol{\Gamma}_x)_j = \phi_{\theta,\tau}^{\text{SBM}} \left(\frac{\boldsymbol{\Gamma}_{j+1} - \boldsymbol{\Gamma}_j}{\boldsymbol{\Gamma}_j - \boldsymbol{\Gamma}_{j-1}} \right) \frac{\boldsymbol{\Gamma}_j - \boldsymbol{\Gamma}_{j-1}}{\Delta x} \quad (\text{A.1})$$

and

$$(\boldsymbol{\Gamma}_x)_{j+1} = \phi_{\theta,\tau}^{\text{SBM}} \left(\frac{\boldsymbol{\Gamma}_{j+2} - \boldsymbol{\Gamma}_{j+1}}{\boldsymbol{\Gamma}_{j+1} - \boldsymbol{\Gamma}_j} \right) \frac{\boldsymbol{\Gamma}_{j+1} - \boldsymbol{\Gamma}_j}{\Delta x}, \quad (\text{A.2})$$

where the two-parameter SBM function

$$\phi_{\theta,\tau}^{\text{SBM}}(r) := \begin{cases} 0, & r < 0, \\ \min\{r\theta, 1 + \tau(r-1)\}, & 0 < r \leq 1, \\ r\phi_{\theta,\tau}^{\text{SBM}}(\frac{1}{r}), & \text{otherwise,} \end{cases} \quad (\text{A.3})$$

is applied in the component-wise manner. Equipped with (A.1) and (A.2), we evaluate

$$\boldsymbol{\Gamma}_{j+\frac{1}{2}}^- = \boldsymbol{\Gamma}_j + \frac{\Delta x}{2}(\boldsymbol{\Gamma}_x)_j \quad \text{and} \quad \boldsymbol{\Gamma}_{j+\frac{1}{2}}^+ = \boldsymbol{\Gamma}_{j+1} - \frac{\Delta x}{2}(\boldsymbol{\Gamma}_x)_{j+1},$$

and then obtain the corresponding point values of \mathbf{U} by $\mathbf{U}_{j+\frac{1}{2}}^\pm = R_{j+\frac{1}{2}} \boldsymbol{\Gamma}_{j+\frac{1}{2}}^\pm$.

Remark A.1 The parameters $\theta \in [1, 2]$ and τ in (A.3) can be used to adjust the amount of numerical dissipation present in the resulting scheme. Generally, larger values of θ lead to sharper but potentially more oscillatory reconstructions. In all of the numerical examples presented in this paper, we have taken $\theta = 2$.

According to [28], the behavior of the SBM limiter depends on τ in the following manner:

- When $\tau \geq 0.5$, the limiter is dissipative, which often leads to strong smearing of contact discontinuities over time;
- For $0 \leq \tau < 0.5$, the limiter is compressive, sharply resolving contact waves within few grid points; however, smooth extrema may be slightly compressed, introducing small kinks in otherwise continuous profiles;
- If $\tau < 0$, the limiter is overcompressive, preserving contact discontinuities sharply over long times but overcompressing smooth regions, possibly producing artificial $\mathcal{O}(1)$ jump discontinuities there.

Remark A.2 The matrices $R_{j+\frac{1}{2}}$ and $R_{j+\frac{1}{2}}^{-1}$ in the case of the Euler equations of gas dynamics can be found in [5, Appendix A].

B 2-D LCD-Based Piecewise Linear Reconstruction

In this appendix, we describe how to reconstruct the one-sided point values $\mathbf{U}_{j+\frac{1}{2},k}^\pm$ (the point values $\mathbf{U}_{j,k+\frac{1}{2}}^\pm$ can be computed in a similar manner and we omit the details for the sake of brevity). To this end, as in the 1-D case, we first introduce the local characteristic variables in the neighborhood of $(x, y) = (x_{j+\frac{1}{2}}, y_k)$:

$$\boldsymbol{\Gamma}_{\ell,k} = R_{j+\frac{1}{2},k}^{-1} \bar{\mathbf{U}}_{\ell,k}, \quad \ell = j-1, j, j+1, j+2,$$

where the matrix $R_{j+\frac{1}{2},k}$ is such that $R_{j+\frac{1}{2},k}^{-1} \hat{A}_{j+\frac{1}{2},k} R_{j+\frac{1}{2},k}$ is diagonal and a locally linearized Jacobian is $\hat{A}_{j+\frac{1}{2},k} := A((\bar{\mathbf{U}}_{j,k} + \bar{\mathbf{U}}_{j+1,k})/2)$.

Equipped with the values $\boldsymbol{\Gamma}_{j-1,k}$, $\boldsymbol{\Gamma}_{j,k}$, $\boldsymbol{\Gamma}_{j+1,k}$, and $\boldsymbol{\Gamma}_{j+2,k}$, we compute

$$(\boldsymbol{\Gamma}_x)_{j,k} = \phi_{\theta,\tau}^{\text{SBM}} \left(\frac{\boldsymbol{\Gamma}_{j+1,k} - \boldsymbol{\Gamma}_{j,k}}{\boldsymbol{\Gamma}_{j,k} - \boldsymbol{\Gamma}_{j-1,k}} \right) \frac{\boldsymbol{\Gamma}_{j,k} - \boldsymbol{\Gamma}_{j-1,k}}{\Delta x},$$

and

$$(\boldsymbol{\Gamma}_x)_{j+1,k} = \phi_{\theta,\tau}^{\text{SBM}} \left(\frac{\boldsymbol{\Gamma}_{j+2,k} - \boldsymbol{\Gamma}_{j+1,k}}{\boldsymbol{\Gamma}_{j+1,k} - \boldsymbol{\Gamma}_{j,k}} \right) \frac{\boldsymbol{\Gamma}_{j+1,k} - \boldsymbol{\Gamma}_{j,k}}{\Delta x},$$

where the SBM function, defined in (A.3), is applied in the component-wise manner. We then use these slopes to evaluate

$$\boldsymbol{\Gamma}_{j+\frac{1}{2},k}^- = \boldsymbol{\Gamma}_{j,k} + \frac{\Delta x}{2} (\boldsymbol{\Gamma}_x)_{j,k} \quad \text{and} \quad \boldsymbol{\Gamma}_{j+\frac{1}{2},k}^+ = \boldsymbol{\Gamma}_{j+1,k} - \frac{\Delta x}{2} (\boldsymbol{\Gamma}_x)_{j+1,k},$$

and finally obtain the corresponding point values of \mathbf{U} by

$$\mathbf{U}_{j+\frac{1}{2}}^\pm = R_{j+\frac{1}{2},k} \boldsymbol{\Gamma}_{j+\frac{1}{2},k}^\pm.$$

Remark B.1 The matrices $R_{j+\frac{1}{2},k}$ and $R_{j+\frac{1}{2},k}^{-1}$ for the 2-D Euler equations of gas dynamics (1.2), (4.2)–(4.3) can be found in [5, Appendix C].

References

- [1] F. ARÀNDIGA, A. BAEZA, AND R. DONAT, *Vector cell-average multiresolution based on Hermite interpolation*, Adv. Comput. Math., 28 (2008), pp. 1–22.
- [2] M. BEN-ARTZI AND J. FALCOVITZ, *Generalized Riemann problems in computational fluid dynamics*, vol. 11 of Cambridge Monographs on Applied and Computational Mathematics, Cambridge University Press, Cambridge, 2003.
- [3] W. BOSCHERI AND M. DUMBSER, *Arbitrary-Lagrangian-Eulerian one-step WENO finite volume schemes on unstructured triangular meshes*, Commun. Comput. Phys., 14 (2013), pp. 1174–1206.
- [4] S. Z. BURSTEIN AND A. A. MIRIN, *Third order difference methods for hyperbolic equations*, J. Comput. Phys., 5 (1970), pp. 547–571.
- [5] A. CHERTOCK, S. CHU, M. HERTY, A. KURGANOV, AND M. LUKÁČOVÁ-MEDVIĐOVÁ, *Local characteristic decomposition based central-upwind scheme*, J. Comput. Phys., 473 (2023). Paper No. 111718.
- [6] A. CHERTOCK, S. CHU, AND A. KURGANOV, *Adaptive high-order A-WENO schemes based on a new local smoothness indicator*, E. Asian. J. Appl. Math., 13 (2023), pp. 576–609.
- [7] S. CHU, M. HERTY, AND A. KURGANOV, *Novel local characteristic decomposition based path-conservative central-upwind schemes*, J. Comput. Phys., 524 (2025). Paper No. 113692.
- [8] S. CHU, A. KURGANOV, AND I. MENSHOV, *New adaptive low-dissipation central-upwind schemes*, Appl. Numer. Math., 209 (2025), pp. 155–170.
- [9] S. CHU, A. KURGANOV, AND R. XIN, *Low-dissipation central-upwind schemes for compressible multifluids*, J. Comput. Phys., 518 (2024). Paper No. 113311.
- [10] S. CHU, A. KURGANOV, AND R. XIN, *New low-dissipation central-upwind schemes. Part II*, J. Sci. Comput., 193 (2025). Paper No. 33.
- [11] J. DEWAR, A. KURGANOV, AND M. LEOPOLD, *Pressure-based adaption indicator for compressible Euler equations*, Numer. Methods Partial Differential Equations, 31 (2015), pp. 1844–1874.
- [12] M. DUMBSER, O. ZANOTTI, R. LOUBÈRE, AND S. DIOT, *A posteriori subcell limiting of the discontinuous Galerkin finite element method for hyperbolic conservation laws*, J. Comput. Phys., 278 (2014), pp. 47–75.
- [13] G. FU AND C.-W. SHU, *A new troubled-cell indicator for discontinuous Galerkin methods for hyperbolic conservation laws*, J. Comput. Phys., 347 (2017), pp. 305–327.
- [14] Z. GAO, Q. LIU, J. S. HESTHAVEN, B.-S. WANG, W. S. DON, AND X. WEN, *Non-intrusive reduced order modeling of convection dominated flows using artificial neural networks with application to Rayleigh-Taylor instability*, Commun. Comput. Phys., 30 (2021), pp. 97–123.
- [15] A. GELB AND E. TADMOR, *Spectral reconstruction of piecewise smooth functions from their discrete data*, M2AN Math. Model. Numer. Anal., 36 (2002), pp. 155–175.
- [16] A. GELB AND E. TADMOR, *Adaptive edge detectors for piecewise smooth data based on the minmod limiter*, J. Sci. Comput., 28 (2006), pp. 279–306.

- [17] E. GODLEWSKI AND P.-A. RAVIART, *Numerical approximation of hyperbolic systems of conservation laws*, Springer-Verlag, New York, second ed., 2021.
- [18] S. GOTTLIEB, D. KETCHESON, AND C.-W. SHU, *Strong stability preserving Runge-Kutta and multistep time discretizations*, World Scientific Publishing Co. Pte. Ltd., Hackensack, NJ, 2011.
- [19] S. GOTTLIEB, C.-W. SHU, AND E. TADMOR, *Strong stability-preserving high-order time discretization methods*, SIAM Rev., 43 (2001), pp. 89–112.
- [20] J.-L. GUERMOND, R. PASQUETTI, AND B. POPOV, *Entropy viscosity method for nonlinear conservation laws*, J. Comput. Phys., 230 (2011), pp. 4248–4267.
- [21] J. S. HESTHAVEN, *Numerical methods for conservation laws: From analysis to algorithms*, Comput. Sci. Eng. 18, SIAM, Philadelphia, 2018.
- [22] S. KARNI, A. KURGANOV, AND G. PETROVA, *A smoothness indicator for adaptive algorithms for hyperbolic systems*, J. Comput. Phys., 178 (2002), pp. 323–341.
- [23] V. A. KOLOTOLOV, A. A. KURGANOV, V. V. OSTAPENKO, N. A. KHANDEEVA, AND S. CHU, *On the accuracy of shock-capturing schemes calculating gas-dynamic shock waves*, Comput. Math. Math. Phys., 63 (2023), pp. 1341–1349.
- [24] V. A. KOLOTOLOV, V. V. OSTAPENKO, AND N. A. KHANDEEVA, *Fifth-order finite-difference scheme in space with increased accuracy in shock influence areas*, Comput. Math. Math. Phys., 65 (2025), pp. 901–916.
- [25] A. KURGANOV AND E. TADMOR, *Solution of two-dimensional Riemann problems for gas dynamics without Riemann problem solvers*, Numer. Methods Partial Differential Equations, 18 (2002), pp. 584–608.
- [26] M. E. LADONKINA, O. A. NEKLIUDOVA, V. V. OSTAPENKO, AND V. F. TISHKIN, *On the accuracy of discontinuous Galerkin method calculating gas-dynamic shock waves*, Dokl. Math., 107 (2023), pp. 120–125.
- [27] R. J. LEVEQUE, *Finite Volume Methods for Hyperbolic Problems*, Cambridge Texts in Appl. Math., Cambridge University Press, Cambridge, UK, 2002.
- [28] K.-A. LIE AND S. NOELLE, *On the artificial compression method for second-order nonoscillatory central difference schemes for systems of conservation laws*, SIAM J. Sci. Comput., 24 (2003), pp. 1157–1174.
- [29] R. LISKA AND B. WENDROF, *Comparison of several difference schemes on 1D and 2D test problems for the Euler equations*, SIAM J. Sci. Comput., 25 (2003), pp. 995–1017.
- [30] R. LÖHNER, *An adaptive finite element scheme for transient problems in CFD*, Comput. Methods Appl. Mech. Eng., 61 (1987), pp. 323–338.
- [31] G. PUPPO AND M. SEMPLICE, *Numerical entropy and adaptivity for finite volume schemes*, Commun. Comput. Phys., 10 (2011), pp. 1132–1160.
- [32] J. QIU AND C.-W. SHU, *On the construction, comparison, and local characteristic decomposition for high-order central WENO schemes*, J. Comput. Phys., 183 (2002), pp. 187–209.

- [33] J. QIU AND C.-W. SHU, *A comparison of troubled-cell indicators for Runge-Kutta discontinuous Galerkin methods using weighted essentially nonoscillatory limiters*, SIAM J. Sci. Comput., 27 (2005), pp. 995–1013.
- [34] V. V. RUSANOV, *Third-order accurate shock-capturing schemes for computing discontinuous solutions*, Dokl. Akad. Nauk SSSR., 18 (1968), pp. 1303–1305.
- [35] C. W. SCHULZ-RINNE, *Classification of the Riemann problem for two-dimensional gas dynamics*, SIAM J. Math. Anal., 24 (1993), pp. 76–88.
- [36] C. W. SCHULZ-RINNE, J. P. COLLINS, AND H. M. GLAZ, *Numerical solution of the Riemann problem for two-dimensional gas dynamics*, SIAM J. Sci. Comput., 14 (1993), pp. 1394–1414.
- [37] J. SHI, Y.-T. ZHANG, AND C.-W. SHU, *Resolution of high order WENO schemes for complicated flow structures*, J. Comput. Phys., 186 (2003), pp. 690–696.
- [38] C.-W. SHU, *Essentially non-oscillatory and weighted essentially non-oscillatory schemes for hyperbolic conservation laws*, in Advanced numerical approximation of nonlinear hyperbolic equations (Cetraro, 1997), vol. 1697 of Lecture Notes in Math., Springer, Berlin, 1998, pp. 325–432.
- [39] C.-W. SHU, *Essentially non-oscillatory and weighted essentially non-oscillatory schemes*, Acta Numer., 5 (2020), pp. 701–762.
- [40] C.-W. SHU AND S. OSHER, *Efficient implementation of essentially non-oscillatory shock-capturing schemes*, J. Comput. Phys., 77 (1988), pp. 439–471.
- [41] C.-W. SHU AND S. OSHER, *Efficient implementation of essentially nonoscillatory shock-capturing schemes. II*, J. Comput. Phys., 83 (1989), pp. 32–78.
- [42] E. F. TORO, *Riemann solvers and numerical methods for fluid dynamics: A practical introduction*, Springer-Verlag, Berlin, Heidelberg, third ed., 2009.
- [43] M. J. VUIK AND J. K. RYAN, *Automated parameters for troubled-cell indicators using outlier detection*, SIAM J. Sci. Comput., 38 (2016), pp. A84–A104.
- [44] W. WANG, C.-W. SHU, H. C. YEE, D. V. KOTOV, AND B. SJÖGREEN, *High order finite difference methods with subcell resolution for stiff multispecies discontinuity capturing*, Commun. Comput. Phys., 17 (2015), pp. 317–336.
- [45] X. WEN, W. S. DON, Z. GAO, AND J. S. HESTHAVEN, *An edge detector based on artificial neural network with application to hybrid compact-WENO finite difference scheme*, J. Sci. Comput., 83 (2020). Paper No. 49.
- [46] P. WOODWARD AND P. COLELLA, *The numerical solution of two-dimensional fluid flow with strong shocks*, J. Comput. Phys., 54 (1988), pp. 115–173.
- [47] Y. ZHENG, *Systems of conservation laws. Two-dimensional Riemann problems*, Progress in Nonlinear Differential Equations and their Applications, Birkhäuser Boston, Inc., Boston, MA, 2001.